FILE COPY

AD A 009848

	1
Solid State Research	**1975**
Prepared for the Department of the Air Force under Electronic Systems Division Contract F19628-73-C-0002 by **Lincoln Laboratory** MASSACHUSETTS INSTITUTE OF TECHNOLOGY LEXINGTON, MASSACHUSETTS	

This technical report has been reviewed and is approved for publication.

FOR THE COMMANDER
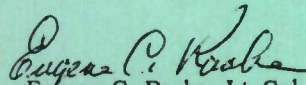
Eugene C. Raabe, Lt. Col., USAF
Chief, ESD Lincoln Laboratory Project Office

MASSACHUSETTS INSTITUTE OF TECHNOLOGY

LINCOLN LABORATORY

SOLID STATE RESEARCH

QUARTERLY TECHNICAL SUMMARY REPORT
TO THE
AIR FORCE SYSTEMS COMMAND

1 NOVEMBER 1974 — 31 JANUARY 1975

ISSUED 17 APRIL 1975

Approved for public release; distribution unlimited.

LEXINGTON   MASSACHUSETTS

ABSTRACT

This report covers in detail the solid state research work
of the Solid State Division at Lincoln Laboratory for the
period 1 November 1974 through 31 January 1975. The
topics covered are Solid State Device Research, Quantum
Electronics, Materials Research, and Microelectronics.
The Microsound work is sponsored by ABMDA and is re-
ported under that program.

CONTENTS

INTRODUCTION

I. SOLID STATE DEVICE RESEARCH

Planar quadrantal arrays of photovoltaic HgCdTe detectors have been fabricated for azimuth and elevation tracking in the ARPA/STO CO_2 laser radar system. ZnS was used as a diffusion mask for an indium-mercury diffusion into p-type material with a 19-percent CdTe alloy composition. These photodiode arrays have shown quantum efficiencies over 50 percent with a uniformity of better than 4 percent.

Electrically active donor impurity concentrations greater than 10^{18} cm^{-3} have been achieved in GaAs by Si-ion implantation. By using a pyrolytic Si_3N_4 encapsulating technique and a post-implantation annealing temperature of 900°C, a peak electron carrier concentration of 8×10^{18} cm^{-3} was measured for a sample implanted with 1×10^{15} Si ions/cm^2.

The measured sheet electron carrier concentration for Se-ion-implanted GaAs has been increased by a factor of five over previously reported values. The Se-ion-implantation dose was 1×10^{14} cm^{-2}; the specimen implantation temperature was 500°C, and the Si_3N_4 encapsulated samples were annealed at 900°C after implantation.

The average power output from external-cavity-operated large optical cavity (LOC) GaAs laser diodes has been increased from about 10 μW to the 1- to 10-mW range. As anticipated from earlier data on external-cavity-operated devices, all the diodes' power was radiated into a line 0.62 Å wide which was tunable over a range of approximately 50 Å.

GaAs varactor diodes are being fabricated for use in K_a-band parametric amplifiers which are to be employed as the first stage in ground-station receivers for the LES-8/9 satellites. These diodes have zero-bias cutoff frequencies in excess of 600 GHz, which should be adequate to meet the system requirements.

II. QUANTUM ELECTRONICS

The threshold and efficiency of a transversely excited, CW, NdP_5O_{14} laser have been measured with 0.58-μm excitation. For a similar configuration, diode-pumped thresholds are calculated to be 4 to 8.5 mW at 0.80 μm, depending on pump bandwidth.

Indium antimonide has been operated continuously as a recombination radiation laser having a single-ended output power of 10 mW when pumped longitudinally with 160 mW of CO laser radiation. About three-orders-of-magnitude greater efficiency was found for longitudinal pumping compared with transverse pumping. Wedge tuning and magnetic-field dependence of the threshold were studied.

For the nonlinear material $CdGeAs_2$, the efficiency of second-harmonic generation has been improved by operation at liquid nitrogen temperature, where carrier concentration is reduced. The change in phasematching angle with temperature has been observed and compared with the measured change in birefringence. Type I phasematching for difference-frequency generation has been measured in $CdGeAs_2$ and $AgGaSe_2$ at room temperature in the 12- to 17-μm region.

Spontaneous spin-flip linewidths in InSb have been measured at high magnetic fields. The results, which are in good qualitative agreement with theory, complete the linewidth studies over the range of carrier concentrations and magnetic fields that are expected to be used in a high-energy pulsed spin-flip laser.

High-energy, narrow-linewidth spin-flip-laser operation has been observed in the 11- to 12-μm range in InSb. At 11.7 μm the maximum single-ended output was 0.6 mJ, while at 12.1 μm the single-ended output was of the order of 0.3 mJ. The linewidth was measured to be less than 0.07 cm^{-1} at the 0.5-mJ output level. Temporal characteristics of the output, as well as magnetic-field tuning properties, were studied.

III. MATERIALS RESEARCH

External quantum efficiencies up to 80 to 85 percent, corresponding to internal quantum efficiencies close to 100 percent, have been achieved for the decomposition of water in optimized photoelectrolytic cells with TiO_2 anodes. These high efficiencies show photoelectrolysis to be a very promising method for the direct conversion of solar energy to chemical energy in the form of gaseous hydrogen.

The electronic structure of TiO_2 and Ti_2O_3 surfaces is being investigated by electron energy-loss spectroscopy in an attempt to elucidate the catalytic behavior of TiO_2 anodes in photoelectrolysis. It is proposed that a triplet of energy-loss peaks observed in the spectra of both compounds is due to transitions from the ground state of the O^{2-} ion to the lowest d-level of Ti, and a strong peak observed only for Ti_2O_3 is attributed to electron transitions between $3d^1$ states of the Ti^{3+} ion.

Films of Sn-doped In_2O_3 with potential applications in the collection and conversion of solar energy have been deposited by RF sputtering on substrates heated by electron bombardment. The electrical conductivity, visible transmission, and infrared reflectivity of these films all increase with increasing substrate temperature, reaching values of about 5×10^3 $(ohm\text{-}cm)^{-1}$, 90 percent, and 95 percent (at 10 μm), respectively, for a substrate temperature of about 650°C.

A reflectometer has been constructed for making absolute measurements of specular reflectance at true normal incidence. This instrument, which also can be used for transmittance measurements, was developed in order to obtain accurate optical data for use in the design and evaluation of transparent heat mirrors for thermal insulation and solar collection.

Dilatometer measurements on oriented single crystals of $AgGaSe_2$, an efficient nonlinear material used for frequency doubling and mixing in the infrared, have shown that the thermal expansion coefficients parallel and perpendicular to the c-axis are negative and positive, respectively. The negative coefficient explains why single crystals grown from the melt by the Bridgman method are always cracked unless the growth axis is within about 20° of the c-axis.

Single-crystal x-ray diffraction analysis has been used to determine the crystal structure of $NdLiP_4O_{12}$, a compound in which we have demonstrated low-threshold, efficient, room-temperature CW laser action. As in other high-Nd-concentration laser materials, including NdP_5O_{14}, concentration quenching of Nd^{+3} fluorescence is greatly reduced in this structure because neighboring Nd^{+3} ions do not share common O^{2-} ions.

IV. MICROELECTRONICS

Several VERS-11 sensors (Visible Earth Radiation Sensors) have been delivered for use in the LES-8/9 satellite project. The final sensor design consisted of four 8-element photodiode arrays mounted on a 2- × 2-inch alumina substrate using conducting epoxy. The substrate was then mounted into an aluminum plate using a vacuum outgassed epoxy, and connection to the external circuitry was made with connectors mounted in the reverse side of the plates. The finished sensors have performed as expected, and have passed the qualification tests required for use on the satellites.

Two significant changes have been made in the fabrication procedure for the silicon charge-coupled device (CCD) imaging arrays to be used in the Telescope Detection and Ranging (TDAR) program. The first change was a final high-temperature anneal of the silicon in H_2, rather than in N_2, which resulted in lowering the fast interface state density from 2×10^{11} to $2 \times 10^{10}\,cm^{-2}eV^{-1}$. The second change involved the deposition of the gate-level polysilicon layers in N_2 rather than H_2, and at a lower temperature (650° to 750°C) rather than 1000°C. The resulting grain size, ~1 μm, is satisfactory for the present device. Measurements of charge transfer efficiency on a 100-element linear CCD fabricated as above with a n-type buried channel have shown inefficiency values as low as 2×10^{-4} per transfer at 1 MHz.

A silicon Schottky barrier diode array has been made for use with a lithium niobate surface acoustic wave (SAW) device to form a memory and correlator structure. The silicon structure, which is $100 \times 800 \times 9$ mils thick, has an array of 0.2-mil-diameter PtSi Schottky barrier diodes on 0.5-mil centers on the active surface, in close proximity to the lithium niobate. The initial device has shown very promising performance, with a storage time of 10 msec for a write time of 50 nsec.

A surface acoustic wave tapped delay line is currently being designed and fabricated for use in the Re-entry Systems Program. The complete line will have 11 output taps of varying delays, with a maximum delay of 66 μsec and a 3-dB bandwidth of 100 MHz. An initial prototype line of smaller delay (7.5 μsec) has been made and evaluated. The line does operate as expected, except for a larger than expected minimum in the response at center frequency. The transducers are currently being modified to minimize this response dip.

REPORTS ON SOLID STATE RESEARCH

15 November 1974 through 15 February 1975

PUBLISHED REPORTS

Journal Articles

JA No.

4272	Electronic Structure of Transition Metals. III. d-Band Resonance and Regge-Pole Theory	A. O. E. Animalu	Phys. Rev. B $\underline{10}$, 4964 (1974)
4310	Comparison of Optical to Injection Excitation in GaAs Heterostructure Lasers	J. A. Rossi S. R. Chinn J. J. Hsieh M. C. Finn	J. Appl. Phys. $\underline{45}$, 5383 (1974)
4358	Heterodyne Measurements of $^{12}C^{16}O$ Laser Frequencies and Improved Dunham Coefficients	H. Kildal R. S. Eng A. H. M. Ross*	J. Mol. Spectrosc. $\underline{53}$, 479 (1974), DDC AD-A006706
4373	Thickness and Surface Morphology of GaAs LPE Layers Grown by Supercooling, Step-Cooling, Equilibrium-Cooling, and Two-Phase Solution Techniques	J. J. Hsieh	J. Cryst. Growth $\underline{27}$, 49 (1974)
4376	Flashlight-Size External Cavity Semiconductor Laser with Narrow-Linewidth Tunable Output	H. Heckscher J. A. Rossi	Appl. Opt. $\underline{14}$, 94 (1975)
4399	Graphite Landau Levels in the Presence of Trigonal Warping	G. Dresselhaus	Phys. Rev. B $\underline{10}$, 3602 (1974), DDC AD-A006314
4400	Horizontal Unseeded Vapor Growth of IV-VI Compounds and Alloys	T. C. Harman J. P. McVittie	J. Electron. Mater. $\underline{3}$, 843 (1974), DDC AD-A006315
4404	Doppler-Limited Molecular Spectroscopy by Difference-Frequency Mixing	A. S. Pine	J. Opt. Soc. Am. $\underline{64}$, 1683 (1974)
4416	Band Structure of $CdGeAs_2$ Near $\vec{k} = 0$	H. Kildal	Phys. Rev. B $\underline{10}$, 5082 (1974)
4418	Doppler-Limited Spectra of the ν_3 Vibration of $^{12}CH_4$ and $^{13}CH_4$	A. S. Pine	J. Mol. Spectrosc. $\underline{54}$, 13 (1975)

---

* Author not at Lincoln Laboratory.

JA No.

4422	Submillimeter Heterodyne Detection and Harmonic Mixing Using Schottky Diodes	H. R. Fetterman B. J. Clifton P. E. Tannenwald C. D. Parker H. Penfield*	IEEE Trans. Microwave Theory Tech. MTT-22, 1013 (1974)
4424	Electroabsorption Avalanche Photodiodes	G. E. Stillman C. M. Wolfe J. A. Rossi J. P. Donnelly	Appl. Phys. Lett. 25, 671 (1974), DDC AD-A006705
4427	Submillimeter-Wave Optically-Pumped Molecular Lasers	H. R. Fetterman H. R. Schlossberg*	Microwave J. 17, 35 (1974)
4429	Effects of Cesiation on Secondary-Electron Emission from MgO/Au Cermets	V. E. Henrich J. C. C. Fan	J. Appl. Phys. 45, 5484 (1974)
4431	Transparent Heat-Mirror Films of $TiO_2/Ag/TiO_2$ for Solar Energy Collection and Radiation Insulation	J. C. C. Fan F. J. Bachner G. H. Foley P. M. Zavracky	Appl. Phys. Lett. 25, 693 (1974)
4437	Double Heterostructure $Pb_{1-x}Sn_xTe$ Waveguides at 10.6 μm	R. W. Ralston J. N. Walpole T. C. Harman I. Melngailis	Appl. Phys. Lett. 26, 64 (1975)
4438	Crystal Structure and Fluorescence Lifetime of $NdAl_3(BO_3)_4$, a Promising Laser Material	H. Y-P. Hong K. Dwight	Mater. Res. Bull. 9, 1661 (1974), DDC AD-A006704
4447	High Resolution Q-Branch Spectrum of CO_2 at 618 cm^{-1}	J. P. Aldridge* R. F. Holland* H. Flicker* K. W. Nill T. C. Harman	J. Mol. Spectrosc. 54, 328 (1975)
4449	Heterodyne Measurements of $^{12}C^{18}O$, $^{13}C^{16}O$, and $^{13}C^{18}O$ Laser Frequencies; Mass Dependence of Dunham Coefficients	A. H. M. Ross* R. S. Eng H. Kildal	Opt. Commun. 12, 433 (1974)

Meeting Speeches

MS No.

3651A	Reliability of Silicon and GaAs K_A-Band IMPATT Diodes	P. Staecker W. T. Lindley R. A. Murphy J. P. Donnelly	In 12th Annual Proceedings, Reliability Physics Symposium (IEEE, New York, 1974), p.293
3750	Performance and Reliability of K_A-Band GaAs IMPATT Diodes	R. A. Murphy W. T. Lindley D. F. Peterson P. W. Staecker	In 1974 IEEE S-MTT International Microwave Symposium Digest of Technical Papers (IEEE, New York, 1974), p.315

* Author not at Lincoln Laboratory.

*   *   *   *   *

UNPUBLISHED REPORTS

Journal Articles

Meeting Speeches[†]

---

* Author not at Lincoln Laboratory.

† Titles of Meeting Speeches are listed for information only. No copies are available for distribution.

ORGANIZATION

SOLID STATE DIVISION

A. L. McWhorter, *Head*
C. R. Grant, *Assistant*

P. E. Tannenwald
H. J. Zeiger

QUANTUM ELECTRONICS

A. Mooradian, *Leader*
P. L. Kelley, *Associate Leader*

Barch, W. E.
Brueck, S. R. J.
Burke, J. W.
Chinn, S. R.
DeFeo, W. E.
Deutsch, T. F.
Eng, R. S.
Fetterman, H. R.
Hancock, R. C.

Heckscher, H.
Kildal, H.
Larsen, D. M.
Mandel, P.*
Menyuk, N.
Moulton, P. F.*
Parker, C. D.
Pine, A. S.

APPLIED PHYSICS

I. Melngailis, *Leader*
T. C. Harman, *Assistant Leader*
W. T. Lindley, *Assistant Leader*

Belanger, L. J.
Bozler, C. O.
Calawa, A. R.
Carter, F. B.
DeMeo, N.
Donnelly, J. P.
Ferrante, G. A.
Groves, S. H.
Hurwitz, C. E.
Krohn, L., Jr.
Leonberger, F. J.*
Lincoln, G. A., Jr.

McBride, W. F.
Murphy, R. A.
Nill, K. W.
Orphanos, W. G.
Paladino, A. E.
Reeder, R. E.
Rossi, J. A.
Spears, D. L.
Stillman, G. E.
Walpole, J. N.
Wolfe, C. M.

ELECTRONIC MATERIALS

J. B. Goodenough, *Leader*
A. J. Strauss, *Associate Leader*

Anderson, C. H., Jr.
Animalu, A. O. E.
Button, M. J.
Delaney, E. J.
Dresselhaus, G.
Dwight, K., Jr.
Fahey, R. E.
Fan, J. C. C.
Feldman, B.
Finn, M. C.
Henrich, V. E.
Hong, H. Y-P.
Hsieh, J. J.
Iseler, G. W.
Kafalas, J. A.
Kolesar, D. F.

LaFleur, W. J.
Landon, S. N.†
Mastromattei, E. L.
Mavroides, J. G.
Mroczkowski, I. H.
Oli, B.*
Owens, E. B.
Palm, B. J.
Pantano, J. V.
Pierce, J. W.
Plonko, M. C.
Reed, T. B.
Tchernev, D. I.
Tracy, D. M.
Zavracky, P. M.

MICROSOUND

E. Stern, *Leader*
R. C. Williamson, *Assistant Leader*

Alusow, J. A.
Brogan, W. T.
Cafarella, J. H.
Dolat, V. S.
Efremow, N., Jr.
Ingebrigtsen, K.

Kernan, W. C.
Li, R. C. M.
Melngailis, J.
Ralston, R. W.
Smith, H. I.

MICROELECTRONICS

A. G. Foyt, *Leader*

Bachner, F. J.
Beatrice, P. A.
Burke, B. E.
Clough, T. F.
Cohen, R. A.
Durant, G. L.
Foley, G. H.

Grant, L. L.
Gray, R. V.
McGonagle, W. H.
Mountain, R. W.
Pichler, H. H.
Smythe, D. L.
Wilde, R. E.

* Research assistant

† Part time

I. SOLID STATE DEVICE RESEARCH

A. PLANAR HgCdTe QUADRANTAL ARRAYS FOR GIGAHERTZ HETERODYNE OPERATION AT 10.6 μm

Planar quadrantal arrays of photovoltaic HgCdTe detectors have been fabricated for azimuth and elevation tracking in the ARPA/STO CO_2 laser radar system. ZnS was used as a diffusion mask for an indium-mercury diffusion into p-type material with a 19-percent CdTe alloy composition. The individual elements of the 280-μm-diameter arrays were delineated by a 20-μm-wide ZnS strip as shown in the photograph in Fig. I-1. A 100-Å layer of indium was sputtered onto the open regions prior to the diffusion process,[1] which gave rise to negligible sheet resistance apparently due to a heavily doped n^+ surface layer. Layers of sputtered indium and gold form the contact pads.
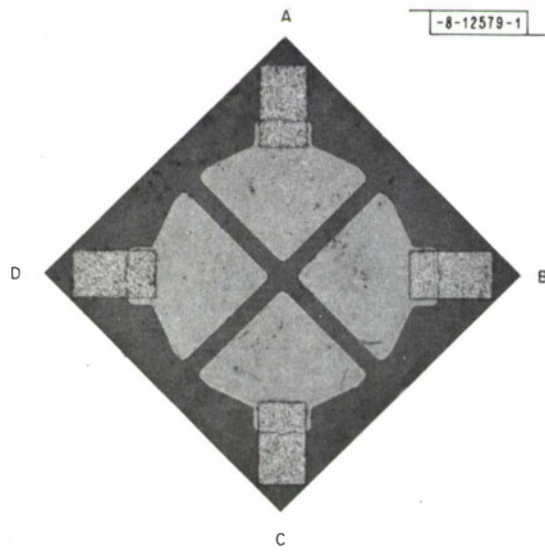
Fig. I-1. Photograph of HgCdTe quadrantal photodiode array.
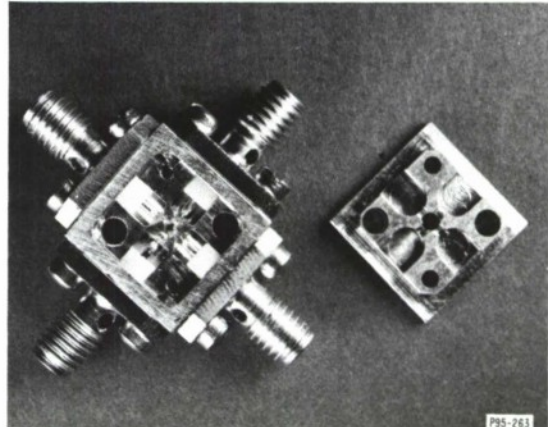
Fig. I-2. HgCdTe photodiode array in microwave package. Cover piece has been removed and inverted to show design details.

The devices were mounted in the microwave package shown in Fig. I-2, which was custom designed to maximize electrical isolation between the connections to the four diodes in the array. A microwave signal, swept from 0.1 to 2 GHz, was fed into one of the array ports, and the signal coming out of the other ports into a 50-ohm load was measured. With the diodes reverse-biased, the leakage signal across adjacent ports was about −50 dB at 0.1 GHz, gradually increased by about 5 dB at 1.5 GHz, and then remained constant to 2 GHz. Opposite ports showed about 5-dB better isolation. When taking into account the input impedance mismatch with a 50-ohm system (due to the ~300-ohm dynamic resistance of the diodes), we calculate over 30-dB electrical isolation between adjacent elements over the 0.1- to 2-GHz range.

The four diodes in each array have shown uniform electrical properties, e.g., in one array the forward impedances ranged from 6 to 7 ohms and reverse impedances varied from

1
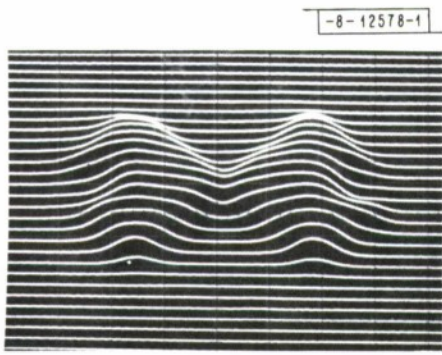
Fig. I-3. CO$_2$ laser raster scan sensitivity profile of HgCdTe quadrantal array with two of the four elements connected to 50-ohm load.
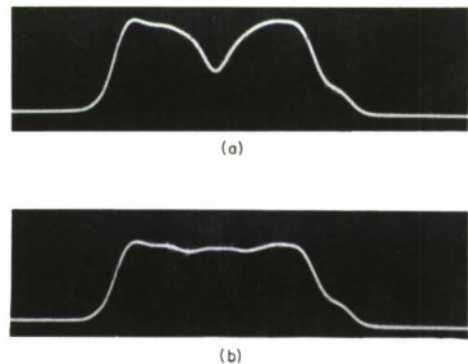
Fig. I-4. Response of HgCdTe quadrantal array to CO$_2$ laser beam scanned across center with (a) two opposite photodiodes connected, and (b) all four photodiodes connected to 50-ohm load.

220 to 400 ohms. In another array the forward impedances ranged from 7 to 11 ohms, while the reverse impedances varied from 250 to 310 ohms. Zero-bias impedances at 77 K ranged from 130 to 150 ohms for these devices, which have a wavelength cutoff of 13.5 μm.

Quantum efficiencies for uncoated devices were in excess of 50 percent at 10.6 μm. Uniformity was determined by raster scanning the arrays with a sharply focused (f/3) CO$_2$ laser beam. A typical pattern is shown in Fig. I-3 where, for clarity, only two of the four devices were connected to the 50-ohm detection circuit. Note the distinct outline of the two quadrature sections and the absence of any signal when the beam scans over the two unconnected devices at the 6- and 12-o'clock positions. The uniformity of the array is more apparent in Fig. I-4(a-b) which shows single scans across the center of the array with two diodes [Fig. I-4(a)] and with all four diodes [Fig. I-4(b)] connected. Note that when all four diodes are connected, the dip in response in the center of the array disappears, indicating very little "dead" region between the four elements. This is consistent with our estimate of 5- to 7-μm diffusion spreading beneath the ZnS mask. The minimum response in Fig. I-4(b) is only about 10 percent less than the maximum signal, corresponding to a ±3-percent variation in quantum efficiency within the 30-μm resolution limit of the scanning optics.

Frequency response and heterodyne minimum detectable power measurements are in progress. Preliminary results indicate a frequency roll-off near 1 GHz.

D. L. Spears

B. ELECTRICAL PROPERTIES OF SILICON ION-IMPLANTED GaAs

In this section, we report results on the implantation of Si into semi-insulating GaAs with high activation (>70 percent) and high electron mobility (>4000 cm^2/V-sec) for a dose of 1×10^{13} cm^{-2}. In addition, a peak n-type carrier concentration of 8.8×10^{18} cm^{-3} and a sheet resistance of 20 Ω/□ has been achieved using a dose of 1×10^{15} cm^{-2}. These results are of major significance to the GaAs microwave and optical device areas.

2

A number of publications that have appeared in the literature deal with the electrical properties of ion-implanted GaAs (Refs. 2 through 11). Although the room-temperature implantation of p-type dopants has yielded high doping efficiencies,[5,8] several publications have indicated that ion implantations into heated GaAs substrates are required to achieve good doping efficiency for the Column VI n-type dopants Se (Refs. 3 and 4) and Te (Refs. 10 and 11). Backscattering measurements of the damage created during ion implantation have indicated that there is an annealing stage at ≈ 300 K (Ref. 9), and implants made into substrates above 150°C have resulted in reduced damage and better doping efficiency for Te ion implants in GaAs (Refs. 10 and 11). Several publications have also shown that silicon-implanted GaAs layers are n-type.[6,7,9]

Several factors have hampered these studies. The most important limitation has been the inability to effectively encapsulate the GaAs at annealing temperatures above about 750°C. Therefore, annealing temperatures either have been limited to temperatures below about 750°C or results have generally not been reproducible. A pyrolytic Si_3N_4 encapsulation system developed at Lincoln Laboratory has reproducibly withstood annealing temperatures up to at least 950°C. Schottky barriers made on n-type GaAs samples before encapsulation, and after encapsulation and annealing at 950°C have given identical capacitance-voltage characteristics. Another less serious problem has been the effective encapsulation of the GaAs during hot implantations. Since 500 to 700 Å of Si_3N_4 is sufficient for encapsulation during annealing at 950°C, implantation can be made through a Si_3N_4 layer of this thickness with the substrate at any temperature up to 950°C. The Si_3N_4 is thin enough so that the peak of the ion distribution of even a 400-kV Te implant will be within the GaAs. The problem of recoil implantation of silicon and nitrogen from the surface coating does not seem to be serious, but will be investigated in the future. It should be noted that this Si_3N_4 encapsulation system has been used successfully in fabricating p-n junction IMPATT diodes using Cd-ion implantation.[12]

For the preliminary Si implantations reported in this section, Cr-doped semi-insulating GaAs was used for the substrates. Care must be taken in using semi-insulating GaAs for ion-implantation studies because the level of compensation in this material usually is not known. The same ingot of semi-insulating GaAs was used for all these experiments. High doping efficiencies were obtained for Si doses of 1×10^{13} cm^{-2}, indicating that substrate parameters are probably not compensating the implanted Si to a large extent. However, these results should be considered to represent a minimum doping efficiency. Implantations will be made into epitaxial material with low compensation after a better understanding of the optimum implant temperature and annealing temperature is achieved. The GaAs substrates were oriented in the {211} direction. After polishing, the samples were free-etched in freshly prepared 5 H_2SO_4: 1 H_2O_2: 1 H_2O. A 500- to 700-Å layer of Si_3N_4 was then pyrolytically deposited on each sample at 720°C.

400-keV Si$^+$ ions were implanted into the GaAs samples which were either at room temperature or 400°C. The Si doses used in these experiments ranged from 1×10^{13} to 1×10^{15} cm^{-2}. After implantation, a 2000-Å SiO_2 layer was pyrolytically deposited at 400°C over the Si_3N_4 for mechanical protection of the Si_3N_4 layer. Anneals were then carried out in a flowing N_2 atmosphere at either 850° or 900°C for 15 minutes.

After annealing, the SiO_2 and Si_3N_4 layers were removed in HF, and a 6000-Å SiO_2 layer was pyrolytically deposited at 400°C. Using photolithographic techniques, Au-Sn contacts appropriate for cloverleaf patterns[3,4] were electroplated on the GaAs implanted layers. These contacts were microalloyed for 1 minute at 420°C to provide good ohmic contact to the implanted layer. Additional Au was electroplated over the Au-Sn after alloying. Cloverleaf patterns were
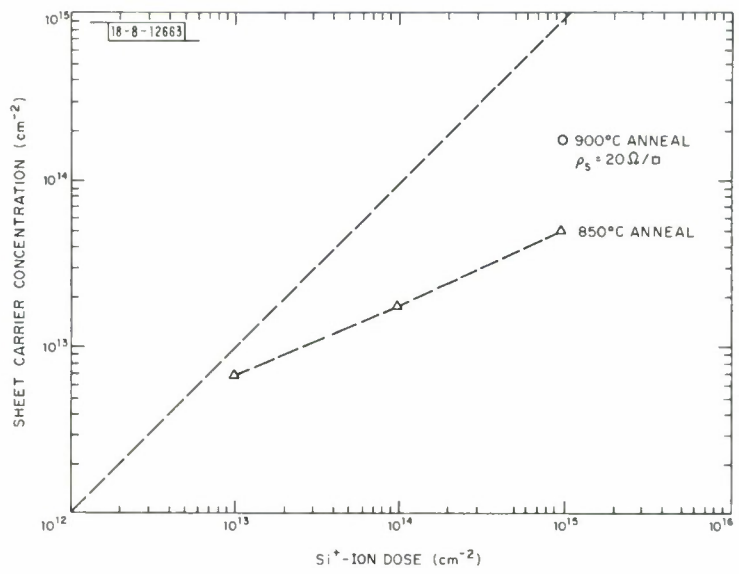
Fig. I-5. Sheet carrier concentration of GaAs layers implanted with 400-keV Si ions at room temperature through 700 Å of Si_3N_4. Straight line represents 100-percent electrical activity.
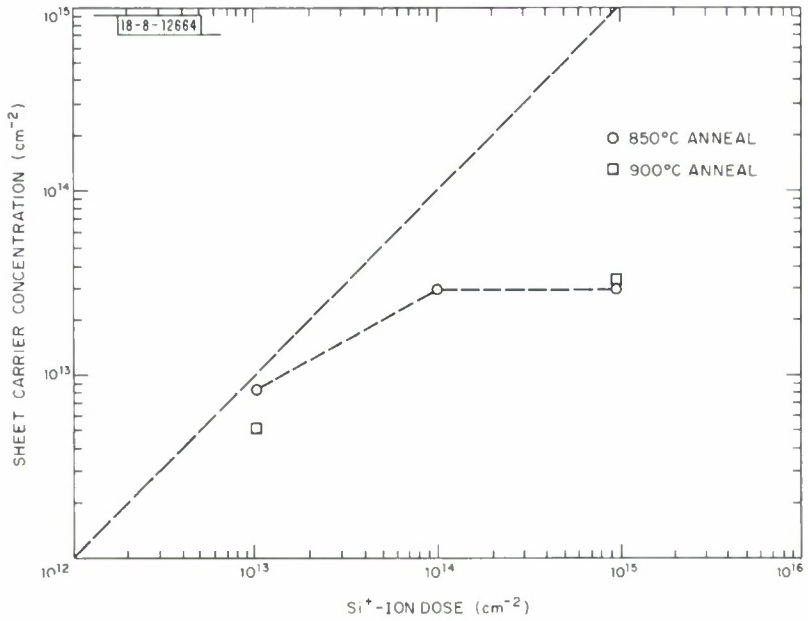

Fig. I-6. Sheet carrier concentration of GaAs layers implanted with 400-keV Si ions at 400°C through 700 Å of Si_3N_4.

4

defined in the oxide to serve as a mask for etching through the implanted layer in order to make Hall measurements of the van der Pauw type.

All the Si implants performed in this work have resulted in n-type conductivity. Figure I-5 shows the effective sheet carrier concentration for implants performed at room temperature. For 850°C anneals, the effective doping efficiency decreases from about 70 percent for a dose of 1×10^{13} cm^{-2} to about 5 percent for a dose of 1×10^{15} cm^{-2}. For a sample implanted with 1×10^{15} Si/cm^2 and annealed at 900°C, the sheet carrier concentration was 1.8×10^{14} cm^{-2} for an effective doping efficiency of 18 percent. The sheet resistivity for this sample was 20 $\Omega/\square$. This is believed to be the lowest sheet resistivity ever reported for an ion-implanted GaAs layer. As discussed in Refs. 3 and 4, these measurements generally underestimate the doping efficiency because (1) some of the ions are stopped in the Si$_3$N$_4$ layer, and (2) variations in the mobility with depth in the implanted layer lead to a measured sheet carrier concentration which is smaller than the actual value.[3,13] Another factor which reduces the measured sheet carrier concentration that has not been previously discussed is the loss of mobile carriers in the surface depletion region usually found in n-type GaAs. This depletion region is due to surface states which pin the Fermi level at the surface at an energy about 2/3 E_g below the conduction band. This effect could reduce the measured sheet carrier concentration in a typical implant of 1×10^{14} cm^{-2} by 10 percent or more.

Figure I-6 shows the effective sheet carrier concentration for samples implanted at 400°C. For samples annealed at 850°C, a Si-ion dose of 1×10^{13} cm^{-2} resulted in a sheet carrier concentration of 8.1×10^{12} cm^{-2} which is slightly higher than that obtained for a room-temperature implant. For a Si-ion dose of 1×10^{14} cm^{-2}, the sheet carrier concentration of 3.0×10^{13} cm^{-2} was also higher than that obtained for a room-temperature implant. For a Si-ion dose of 1×10^{15} cm^{-2}, however, the sheet carrier concentration of 3×10^{13} cm^{-2} was lower than that obtained for a room-temperature implant.

When the anneal temperature was increased to 900°C, the sheet carrier concentration for a sample implanted with 1×10^{13} Si/cm^2 decreased to 5.1×10^{12} cm^{-2}. For a sample implanted with 1×10^{15} Si/cm^2, the sheet carrier concentration increased only minimally to 3.3×10^{13} cm^{-2}, which is over a factor-of-5 less than obtained for a room-temperature implantation.

Table 1-1 summarizes the results obtained to date and includes the integrated carrier concentrations obtained from a series of etching steps and Hall measurements.[7] A 1 H$_2$SO$_4$: 1 H$_2$SO$_4$: 50 H$_2$O etch immersed in an ice bath was used for etching the steps. A surface profiler was used to measure the total etch depth at periodic intervals. For 1-minute etch times, the average etch rate was nominally 300 Å/minute. There was some indication that the etch rate was slightly faster near the surface, but the difference was not sufficient to reach any definite conclusions. Only the center portion of the cloverleaf pattern was etched. Hall measurements were made after each etch step, but only the data which resulted in sheet carrier concentration differences larger than the experimental error were used in calculating the carrier concentration and mobility as a function of depth.

The carrier concentration profiles measured on the GaAs samples implanted at room temperature and annealed at 850°C are shown in Fig. I-7. Also shown is the mobility profile for the sample implanted with 1×10^{15} cm^{-2}. The projected range of 400-keV Si$^+$ ions in GaAs (subtracting 700 Å for the Si$_3$N$_4$ layer) is about 2800 Å and is indicated in Fig. I-7. For the samples implanted with 1×10^{14} and 1×10^{15} cm^{-2}, it appears that only the Si ions which penetrated deeper than the projected range are being incorporated efficiently as donors

TABLE I-1						
SUMMARY OF RESULTS FOR 400-kV Si⁺-ION IMPLANTATION IN GaAs						
Dose (cm^{-2})	Temperature of Implant (°C)	Anneal Temperature (°C)	Sheet Carrier Concentration (cm^{-2})	Sheet Mobility (cm^2/V-sec)	Sheet Resistivity (Ω/□)	Etch Step Integrated Concentration (cm^{-2})
1×10^{13}	25	850	6.9×10^{12}	4220	213	7.0×10^{12}
1×10^{14}	25	850	1.8×10^{13}	3110	112	2.7×10^{13}
1×10^{15}	25	850	5.2×10^{13}	2000	60	9.4×10^{13}
1×10^{15}	25	900	1.8×10^{14}	1750	20	2.0×10^{14}
1×10^{13}	400	850	8.1×10^{12}	4105	187	—
1×10^{13}	400	900	5.1×10^{12}	4240	288	—
1×10^{14}	400	850	3.0×10^{13}	2815	75	—
1×10^{15}	400	850	3.0×10^{13}	2380	87	—
1×10^{15}	400	900	3.3×10^{13}	2690	70	—
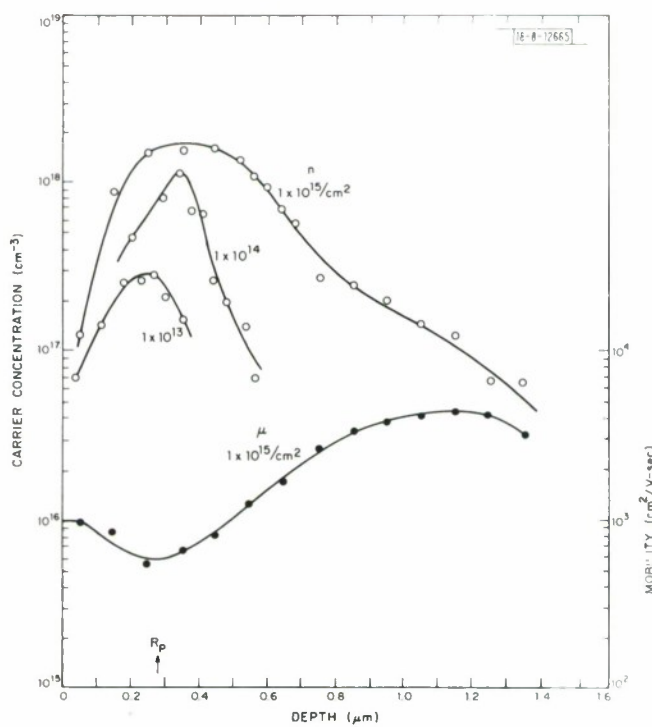
Fig. I-7. Carrier concentration and mobility vs depth measured in GaAs implanted with 400-keV Si ions at room temperature through 700 Å of Si$_3$N$_4$ and annealed at 850°C.
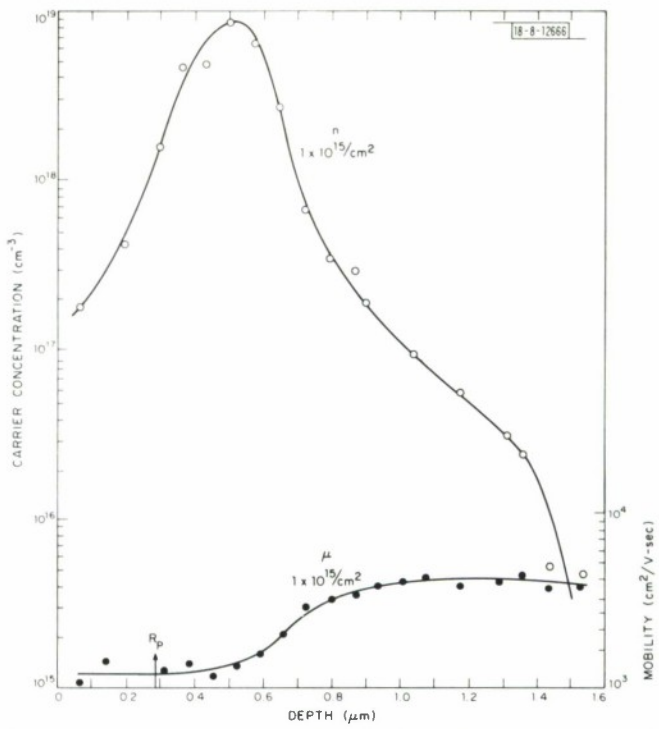
Fig. I-8. Carrier concentration and mobility vs depth measured in GaAs implanted with 400-keV Si ions at room temperature through 700 Å of Si_3N_4 and annealed at 900°C.

in the GaAs. The deeply penetrating tail on the sample implanted with 1×10^{15} cm^{-2} could be due to enhanced diffusion or channeling. Figure I-8 shows the carrier concentration and mobility profiles obtained for the sample implanted with 1×10^{15} Si/cm^2 and annealed at 900°C. The peak carrier concentration occurs at about 0.48 µm and is 8×10^{18} cm^{-3}. The silicon atoms close to the surface are still not incorporated efficiently as donors. This could be due to residual damage, self-compensation, or most probably a combination of both. The deeply penetrating tail on this sample is, if anything, smaller than that found in the sample annealed at 850°C. If this tail is due to enhanced diffusion, this may indicate that the diffusion is taking place during the implant. For device applications, 3000 Å easily could be etched off the surface of this sample with only a negligible increase in the sheet resistivity. This would move the surface past any residual damage and self-compensation and into a region of electron concentration greater than 10^{18} cm^{-3}.

Additional experiments are in progress so that a better understanding of Si implantation in GaAs can be achieved. The results reported in this section show that GaAs implanted with Si at room temperature and annealed at 900°C can result in n-type layers with sheet resistivities as low as 20 Ω/□. Microwave FETs with high-performance uniformity and yield should be possible using the light implants to form the active layer, and the heavy-dose implants for ohmic contacts.

<div align="right">

J. P. Donnelly
W. T. Lindley

</div>

C. ELECTRICAL PROPERTIES OF SELENIUM ION-IMPLANTED GaAs

We previously reported efficient doping of GaAs by Se ion implantation.[3,4] That work was limited to anneal temperatures of 800°C because of the SiO_2 used to encapsulate the GaAs. In this section, we report some new results on Se implants using the Si_3N_4 encapsulating technique described in the preceding section. The GaAs substrates and sample preparation techniques used in these experiments were also the same as described in the preceding section. The implantations were made through a 500- to 700-Å layer of Si_3N_4 at substrate temperatures ranging from room temperature to 500°C. The implant dose was 1×10^{14} cm^{-2}, and the samples were annealed at 900°C for 15 minutes following implantation.
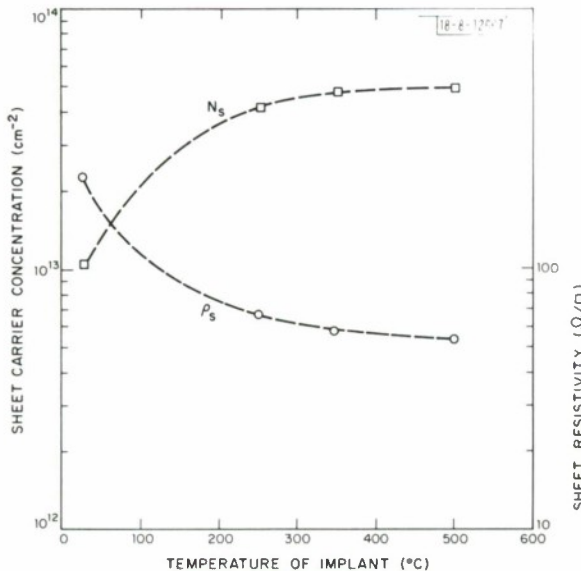
Fig. I-9. Sheet carrier concentration and sheet resistivity vs temperature of implant for 400-keV Se$^+$ ion-implanted GaAs annealed at 900°C. Implant dose was constant at 1×10^{14} cm^{-2}, and implants were made through 700 Å of Si_3N_4.

Figure I-9 shows the measured sheet carrier concentration and sheet resistivity as a function of implant temperature. For a room-temperature implant, the sheet carrier concentration was 1.03×10^{13} cm^{-2}. For a 250°C implant, this increased to 4.06×10^{13} cm^{-2}, and further increased to 4.70×10^{13} cm^{-2} for a 350°C implant and to 4.99×10^{13} cm^{-2} for a 500°C implant. The large increase in sheet carrier concentration between the room-temperature and 250°C implant is probably due to the annealing of damage during implantation. An anneal stage at 150°C has been reported for GaAs (Ref. 10). Rough estimates of the implant depths were obtained when etching the cloverleaf patterns by periodically measuring the resistance between two cloverleaves. A surface profiler was used to measure the depth when this resistance increased to several hundred kilohms. This measurement gives an estimate of the extent of any deeply penetrating tail that exists on the implanted distribution. (The range of 400-kV Se$^+$ in GaAs through a 700-Å Si_3N_4 layer is about 0.07 μm with a standard deviation of about 500 Å.) The depth determined in this manner was 0.28 μm for room-temperature implants, 0.61 μm for 250°C implants, 0.77 μm for 350°C implants, and 0.82 μm for 500°C implants. The increased depth with implant temperature is believed to be due to diffusion during the implant itself, and could explain the increase in sheet concentration from 4.06×10^{13} cm^{-2} to 4.99×10^{13} cm^{-2} as the implant temperature is increased from 250° to 500°C. The sheet mobility was 2414 cm^2/V-sec for the room-temperature implant, 2300 for the 250°C implant, 2322 for the 350°C implant, and 2293

for the 500°C implant. As shown in Fig. I-9, the sheet resistivity decreased from 252 $\Omega/\square$ for the room-temperature implant to 54 $\Omega/\square$ for the 500°C implant.

It should be noted that the sheet concentration for a 500°C, 1×10^{14} cm^{-2} implant is about five times higher than that previously reported,[3,4] and the sheet resistivity is about five times lower.

Additional measurements including profiling using stripping techniques are in progress.

J. P. Donnelly

D. EXTERNAL-CAVITY-OPERATED LOC LASER DIODES

We previously reported[14] the operation of GaAs heterostructure diodes in an external dispersive cavity. Throughout the previous work, the diodes were operated with a rectangular (100-nsec), low-duty-cycle (100-Hz), current pulse. Since most diodes radiated about 1 W peak power, the average power radiated was only about 10 μW. Therefore, for applications which require a higher average-power output, e.g., 1 to 10 mW, some modifications are necessary. The requisite changes, which result in 1 to 10 mW average power, are discussed in this report.

The most important modification was made to the current pulser. If the diode radiates about 1 W peak power, a current pulser operating at ~1-percent duty cycle is required to achieve 1 to 10 mW average power. Since the diodes typically had about 4-A thresholds, the current pulser also should be capable of delivering up to 8 A at this duty cycle. A circuit using two RF power transistors previously has been shown to be appropriate for this application,[15] and we have used the circuit with some slight modifications in the present experiments. If this circuit was used for conventional diodes, the diode could be mounted in the center of a PC board to minimize lead lengths. In our applications, however, optical access to both diode faces was required and some relocation of the circuit elements therefore was necessary. The completed circuit package, without power supplies or coolant lines, is shown in Fig. I-10. The material fabricated into diodes was a large optical cavity (LOC) heterostructure wafer; conventional laser diodes made from this wafer radiated 20 mW average power, and thus were suitable for the external cavity requirements.

Fig. I-10. Driving circuit used to obtain high current (~10A) at high duty cycles (~1 percent). Power supplies, trigger, and coolant flow lines are not shown. Diode is mounted in upper right-hand corner and, in operation, whole assembly was cooled by flowing methanol through 1/4-inch-thick copper plate to which power transistors and laser diode are heat sunk.
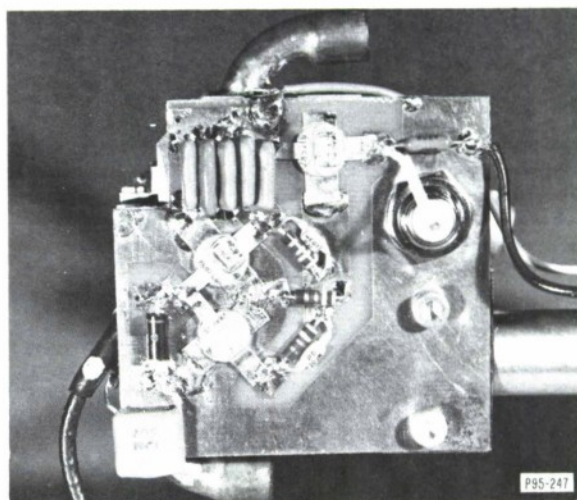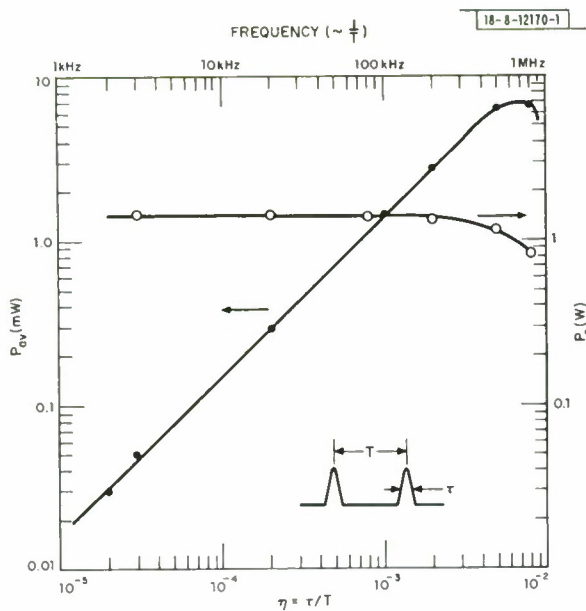
Fig. I-11. Measured peak (P_O) and average (P_{av}) output powers obtained using external cavity and high-duty-cycle pulser shown in Fig. I-10.

DRAWING NOT TO SCALE
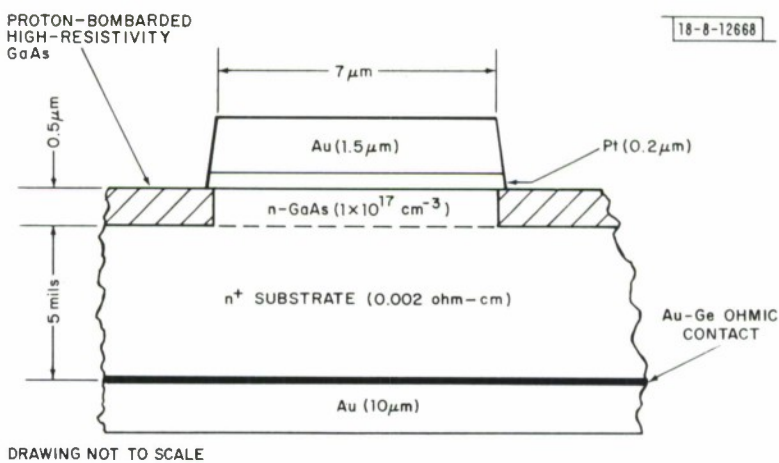
Fig. I-12. GaAs Schottky-barrier varactor diode.

In Fig. I-11 we show the peak (P_o) and average (P_{av}) output powers from a typical device as a function of duty cycle η. Experimentally, the peak radiated power is measured using a calibrated vacuum photodiode and then multiplied by the duty cycle (η = the measured width of the light pulse in the time domain τ, divided by the period between light pulses T) to obtain the average power. For this diode, 6.7 mW average power was obtained at η = 0.008. A further increase in the current drive duty cycle, by increasing the repetition rate, results in a reduction of the width of the diode output pulse in the time domain so that, overall, the duty cycle used to compute the average power is unchanged. For this latter reason and because increasing the repetition rate lowers the peak output power, the descent of the P_{av} curve in Fig. I-11 to the right of the maximum is practically straight down. At this maximum average-power output, the overall circuit efficiency, which is defined as the average radiated power divided by power dissipated by the driving circuit, was 0.15 percent. As expected from earlier external cavity data, the diode radiated all its power into a line 0.62 Å wide which was tunable over a range ~50 Å. With some further modifications in the heat sinking of the diode and by using a lower threshold device, it may be possible to obtain about 30 mW average power radiated into a narrow tunable line.

<div align="right">J. A. Rossi</div>

E. GaAs VARACTOR DIODES FOR K_a-BAND PARAMETRIC AMPLIFIERS

GaAs Schottky-barrier varactor diodes having zero-bias cutoff frequencies of 600 GHz have been fabricated for use in K_a-band parametric amplifiers. These amplifiers are to be used as the first stage in ground-station receivers for the LES-8/9 satellites. The design requirement of the amplifier noise figure is 2.8 dB or less, with a gain of 15 dB at 37.5 GHz.

A cross-sectional view of a typical device is shown in Fig. I-12. The starting material for most of the devices has been liquid-phase n/n^+ epitaxial GaAs grown in-house, although several device wafers have been fabricated from commercially obtained vapor-phase epitaxial GaAs. The epitaxial wafers are characterized by differential capacitance measurements. Wafers of epitaxial material with layer thicknesses of approximately 0.5 μm and electron densities near 1×10^{17} cm^{-3} have been used. The device characteristics measured thus far have indicated little difference in the two types of materials.

The first step in the fabrication procedure is to coat the epitaxial layer with approximately 4500 Å of pyrolytic SiO_2 which serves as a protective cover; then the substrate side of the wafer is lapped to a thickness of 4 to 5 mils. A 500-Å-thick layer of eutectic AuGe is then sputter-deposited upon the substrate, and alloyed in a hydrogen atmosphere to which gaseous HCl has been added. An alloying cycle in which the temperature is linearly varied from 375° to 475°C over a 30-sec interval followed by rapid cooling has thus far yielded the best ohmic contacts. After the alloying cycle, a layer of gold is electroplated over the alloyed region to a thickness of 10 μm (the plated gold layer adds substantially to the mechanical strength of the thin wafer).

After the protective layer of SiO_2 is removed, 0.2 μm of platinum followed by 1.5 μm of gold and 800 Å of titanium is sputtered upon the epitaxial side. Device patterns are photolithographically defined in the titanium layer, and the titanium is used as a mask against RF sputter-etching in a 10-μm Ar, 1-μm O_2 atmosphere. A power of about 50 W is used resulting in a measured 700 V DC on the 6-inch-diameter substrate holder. Because of the presence of oxygen, the titanium etch rate is only 3 Å/minute; thus, the titanium mask easily stands up to the 102 minutes of sputter-etching required to completely remove the exposed areas of Au and Pt. The remaining
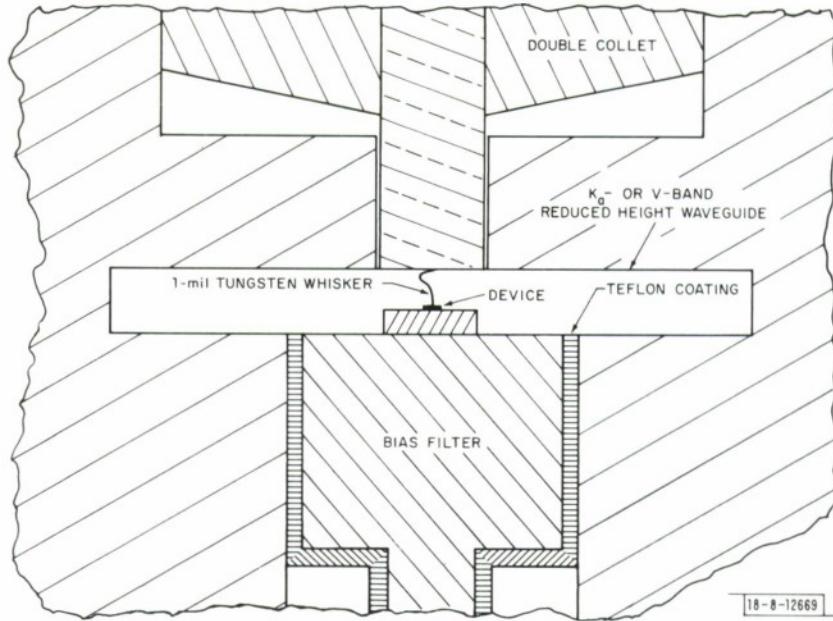
Fig. I-13.   Sharpless wafer mount.

titanium is chemically removed with a 5-pereent HF aqueous solution after the sputter-etching
is completed.   Most of the wafers fabricated have had honeycomb arrays of tightly spaced devices
with diameters of about 7 μm.   Typically, there are 400 devices on a 20- $\times$ 20-mil^2 chip.

After the metalization has been patterned, the wafer is bombarded by a 1×10^{14} cm^{-2} dose
of 50-keV protons to passivate the exposed GaAs regions, and to increase the deviees' breakdown
voltages.   These guarded platinum Schottky-barrier devices have breakdown voltages ranging
from 12 to 15 V, depending on the epitaxial wafer carrier density, and have had zero-bias capac-
itances near 0.06 pF.

The devices have been tested in both K_a- and V-band Sharpless[16] wafer mounts.   Figure I-13
illustrates how the deviccs are contaeted in these mounts.   After the device chip is alloyed to the
Teflon-coated bias pin, it is inserted into the Sharpless wafer mount, and a device is contacted
with 1-mil-diameter gold-plated tungsten wire whose tip has becn pointed to a radius of 5 μm.
The contacting procedure is a delicate one, requiring both visual observation of the contacting
process and the monitoring of the current-voltage characteristic at the Sharpless mount bias port.

Device parameters have thus far becn cvaluated by two techniques: by Deloach resonance[17]
at V-band, and by network analyzer measurements[18] at K_a-band.   In the V-band measurements,
the device is mounted and contacted in a V-band, reduced-height-waveguide (148 $\times$ 15 mil^2)
Sharpless mount.   The transformations to and from full-sized V-band waveguide were effected
by a two-wavelength cosine taper transformer.   The combination of the contacting whisker and
devicc forms a series RLC connection, which at resonance greatly reduccs the microwavc signal
transmitted through the Sharpless wafer.   The resonant frequency, bandwidth, and absolute trans-
mission loss at resonance thus can bc used to infer the tungsten whisker inductance, device ca-
pacitance, and device series resistance.   Series resistances of 4 to 5 ohms with associated zero-
bias cutoff frequencies in excess of 600 GHz have been measured with this technique.

12

In the K_a-band measurements, the devices were mounted and contacted in 280×20 mil^2 or 280×30 mil^2 reduced-height-waveguide Sharpless mounts. The mount is backed by an appropriately positioned short circuit presenting an open circuit at the device reference plane, and the impedance looking into the mount is measured by a K_a-band network analyzer. Figure I-14 shows the results of measurements made in such a configuration, and in particular is a plot of the impedance locus on Smith-chart coordinates as the device bias voltage is varied at constant frequency. Kurokawa[18] has shown that any lossless two-part network can be modeled as shown in the dashed box in the figure. Consequently, it is easy to show that if R_s is independent of bias voltage, the impedance locus seen by the network analyzer always can be rotated onto a constant resistance circle on the Smith chart, and that the fully pumped dynamic quality factor $\tilde{Q}$ (see Ref. 19) can be obtained directly from this locus. In particular, referring to Fig. I-14,

$$
\tilde{Q} \equiv \frac{1/C_{min} - 1/C_{max}}{4\omega R_s} = \frac{(X/Z_o)_{max} - (X/Z_o)_{min}}{4(R/Z_o)} \quad .
$$

The data of Fig. I-14 yield a dynamic $\tilde{Q}$ of approximately 5 and, making use of the device's measured low-frequency capacitance-voltage relationship, yield a series resistance of 5.5 Ω and a zero-bias cutoff frequency of 530 GHz.

The characterization of a device by either of these techniques does have some uncertainties due to whisker contact resistance and possible circuit loss. Measurements indicate that the circuit loss can be neglected in this case, but we have observed that inadequate contact pressure can add as much as 4 Ω to the measured series resistance. However, better contacting procedures have reduced the scatter in series resistance measurements made on similar devices to within 1 Ω and improved the correlation with V-band measurements to within 2 Ω, with the K_a-band network analyzer measurements typically being the more pessimistic.

Since standard estimates of the achievable noise figure and gain of parametric amplifiers indicate that system requirements can be achieved with devices of this quality, the current emphasis is on improving contacting and packaging techniques, and in fabricating circuit elements near the device which will yield proper parametric amplifier operation.

R. A. Murphy   J. Hsieh
W. T. Lindley   G. A. Lincoln
G. Berk
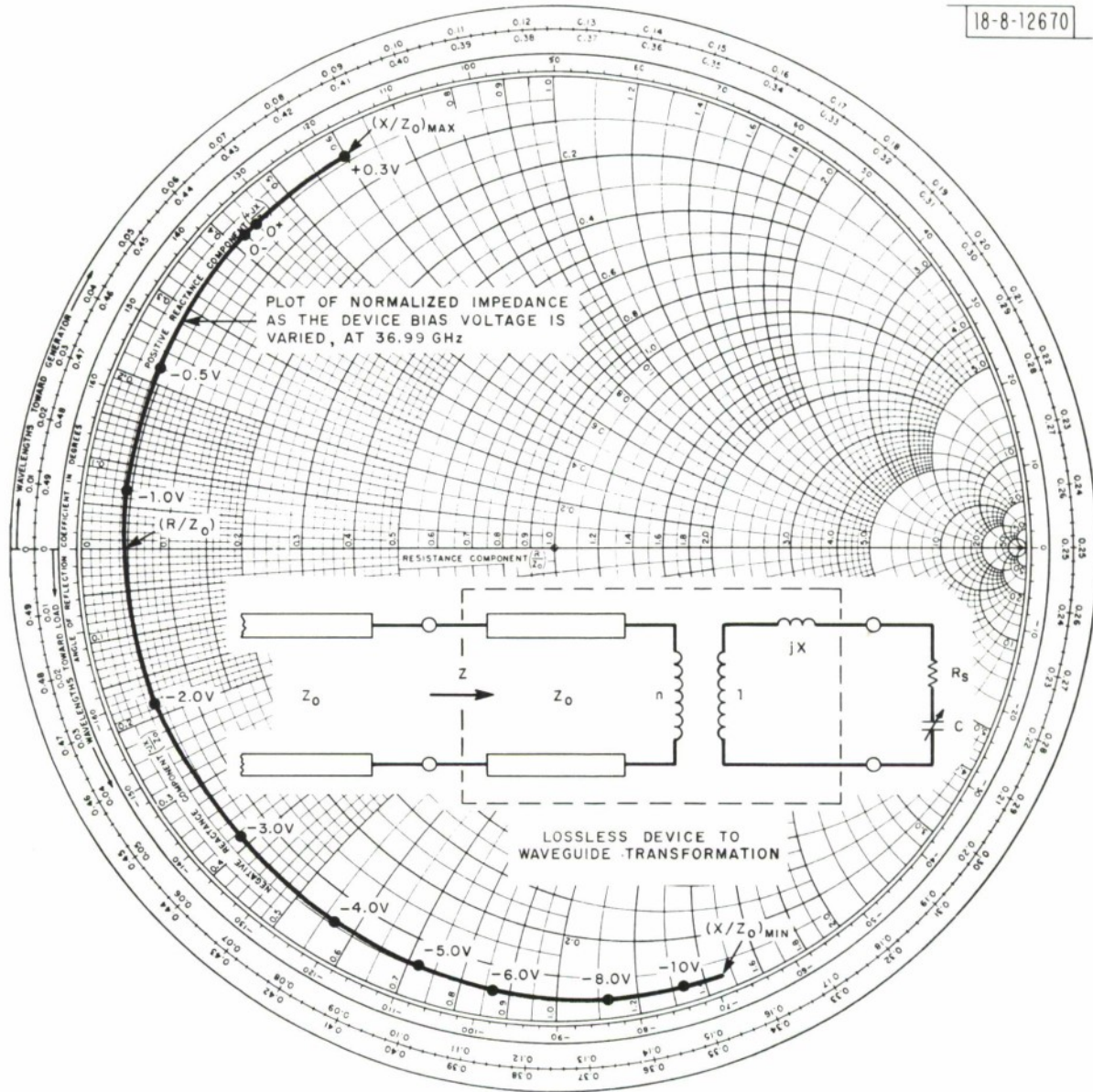
Fig. I-14. Impedance measurement at K_a-band of mounted and contacted device.

REFERENCES

1. Solid State Research Reports, Lincoln Laboratory, M.I.T. (1973:2), p. 2, DDC AD-766233/1; and (1974:4), p. 5, DDC AD-A004763.

2. J. Mayer, O.J. Marsh, R. Mankarious and R. Bower, J. Appl. Phys. $\underline{38}$, 1975 (1967).

3. Solid State Research Report, Lincoln Laboratory, M.I.T. (1969:1), p. 3, DDC AD-687100.

4. A.G. Foyt, J.P. Donnelly and W.T. Lindley, Appl. Phys. Lett. $\underline{14}$, 372 (1969), DDC AD-699465.

5. R.G. Hunsperger and O.J. Marsh, Radiation Effects $\underline{6}$, 263 (1970).

6. J.D. Sansbury and J.F. Gibbons, Appl. Phys. Lett. $\underline{14}$, 311 (1969).

7. _____, Radiation Effects $\underline{6}$, 269 (1970).

8. R.G. Hunsperger, R.G. Wilson and D.M. Jamba, J. Appl. Phys. $\underline{43}$, 1318 (1972).

9. J.S. Harris, in Proceedings of the Conference on Ion Implantation in Semiconductors, Garmisch, 1971 (Springer-Verlag, Berlin, 1971), p. 157.

10. J.S. Harris, F.H. Eisen, B. Welch, J.D. Haskell, R.D. Pashly and J.W. Mayer, Appl. Phys. Lett. $\underline{21}$, 601 (1972).

11. F.H. Eisen, J.S. Harris, B. Welch, R.D. Pashly, D. Sigurd and J.W. Mayer, Proc. Conf. on Ion Implantation in Semiconductors and Other Materials, Yorktown Heights, 1973 (Plenum Press, New York, 1973), p. 631.

12. Solid State Research Report, Lincoln Laboratory, M.I.T. (1973:4), p. 1, DDC AD-778086/9.

13. P.L. Petritz, Phys. Rev. $\underline{110}$, 1254 (1956).

14. J.A. Rossi, S.R. Chinn and H. Heckscher, Appl. Phys. Lett. $\underline{23}$, 25 (1973), DDC AD-771902/4.

15. J.T. O'Brien, United States Army Electronics Command (ECOM) Research and Development Technical Report ECOM-0062-3 (March 1974).

16. W.M. Sharpless, Trans. IRE, PGMTT $\underline{MTT-9}$, 6 (1961).

17. B.C. Deloach, Jr., Trans. IEEE, PTGMTT $\underline{MTT-12(1)}$, 15 (1964).

18. K. Kurokawa, Bell System Tech. J. $\underline{41}$, 361 (1962).

19. H.A. Watson, Ed., Microwave Semiconductor Devices and Their Applications (McGraw-Hill, New York, 1969).

II. QUANTUM ELECTRONICS

A. LOW-THRESHOLD, TRANSVERSELY EXCITED NdP_5O_{14} LASER

We have measured room-temperature CW lasing thresholds of NdP_5O_{14} (NdPP) excited by a dye laser. The pump beam was incident on the sample in a direction perpendicular to the lasing axis, simulating the geometry for excitation by a narrow-junction, edge-emitting LED or laser diode.

The NdPP laser crystal was located at the center of a nearly spherical optical cavity having mirrors with nominally 100- and 99.7-percent reflectivity at the lasing wavelength, 1.052 μm. The pump radiation was focused on the side of the sample by two crossed cylindrical lenses to form a narrow line image parallel with the NdPP laser mode. By tuning the Rhodamine 6G dye laser about the wavelength of peak absorption at 0.580 μm, we have measured the threshold as a function of pump wavelength from 0.575 to 0.590 μm. Typical minimum thresholds were 4 mW at the absorption line center, increasing to 25 mW at wavelengths 0.01 μm away (Fig. II-1). With 20-percent duty-cycle, quasi-CW excitation, we have measured power-conversion efficiencies of ~8 percent at output powers of ~3 mW.
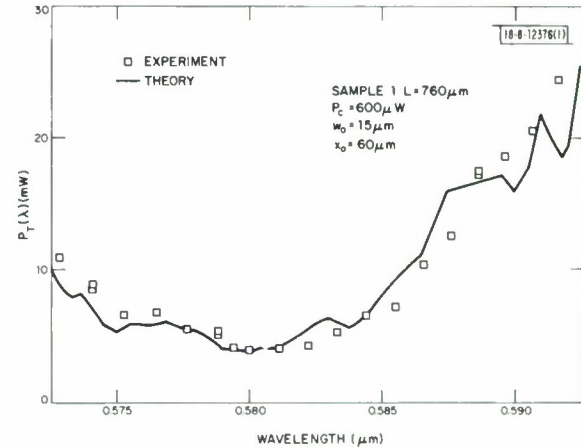
Fig. II-1. Experimental and theoretical transverse pump threshold $P_T(\lambda)$ as a function of wavelength near 0.58 μm for NdPP sample 1, 760 μm long.

Using a simple theoretical model, we have obtained a good fit to the experimental data for threshold vs pump wavelength. In this treatment, the calculated transverse threshold $P_T(\lambda)$ was normalized to the experimentally measured collinear-pumping threshold at 0.58 μm, P_C (typically six times smaller than the transverse value). Using measured values for the pump absorption coefficient and adjustable parameters for the laser mode waist w_0 and depth x_0 inside the crystal, we calculated the values of $P_T(\lambda)$ shown in Fig. II-1 (the results were relatively insensitive to the choice of w_0 and x_0 over a wide range of these parameters). This analysis then was used to calculate thresholds for wider-bandwidth pump sources (such as LEDs or laser diodes) emitting near 0.80 μm, a favorable wavelength for electroluminescent device operation and the location of the strongest absorption band in NdPP. The threshold-vs-pump-bandwidth calculations for the dye-laser configuration are shown in Fig. II-2. Taking account of the larger pump beam divergence from a semiconductor light source placed next to the laser crystal, we estimated that thresholds ranging from 4 mW for an extremely narrowband laser pump, to 8.5 mW for a 300 Å (FWHM) bandwidth LED, should be attainable with our present 760-μm-long NdPP sample.

17
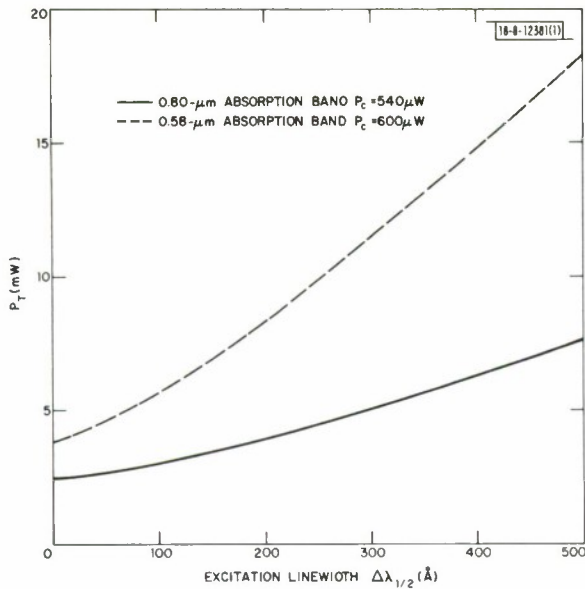
Fig. II-2. Theoretical transverse pump threshold vs FWHM excitation bandwidth $\Delta\lambda_{1/2}$ for NdPP sample 1 using tightly focused pump beam.

We have also succeeded in lowering the threshold and increasing the laser efficiency by using a thin NdPP sample mounted on an aluminized surface which reflected any transmitted pump radiation back into the sample. With this arrangement a transverse threshold (at 0.58 μm) of 2.7 mW was obtained, with a reduction of 60 percent in the ratio of transverse/collinear threshold. A sample only 36 μm thick also lased in this configuration, indicating a possible compatibility with integrated optical technology.

S. R. Chinn
J. W. Pierce
H. Heckscher

B. EFFICIENT InSb LASER WITH RESONANT LONGITUDINAL OPTICAL PUMPING

In a previous study of optical pumping of semiconductor lasers in a transverse geometry, it was shown that CW GaAs pumping of InSb leads to a convenient tunable infrared laser source.[1] Doppler-limited spectroscopy of nitric oxide, ethylene, and water vapor in the 5.3-μm region was demonstrated with this laser. The transverse pumped InSb typically yielded 1- to 10-μW output power for an incident power of 20 to 200 mW.

Much more efficient optical conversion has now been achieved by near-resonant excitation in a longitudinal geometry where the parallel incident radiation and stimulated emission are normal to the polished InSb platelet faces. A single-ended CW output of up to 10 mW has been obtained in a single longitudinal Fabry-Perot mode with an incident CO laser power of 160 mW. This is almost a thousand times more output power than for the transverse geometry. An external quantum efficiency of ~21 percent is calculated from the double-ended output power divided by the absorbed incident power $2P_{out}/(1 - R)P_{in}$, where the reflectivity $R \simeq 44$ percent. Thresholds for the two geometries are comparable (10 to 20 mW), and the emission frequencies are 20 to 30 cm^{-1} higher for longitudinal pumping. Magnetic-field effects on the threshold and emission frequencies are similar for the two pumping schemes.

Previous experiments involving longitudinal pumping of semiconductors[2,3] established that the platelet thickness L should be less than the carrier diffusion length or the pump light absorption depth. In addition, the Fabry-Perot mode spacing, $\Delta\nu_L = 1/2\eta^*L$, should not be larger

18

than the spontaneous emission gain bandwidth. For InSb at T ~ 4.2 K, the latter requires a minimum thickness ~200 μm, which is several times the carrier diffusion length. It is therefore necessary to resonantly pump near the absorption edge of the crystal. Single-mode operation is easily achieved for platelets near the minimum thickness.

1. Experiment

The InSb platelet samples were prepared from ~1-cm^2 wafers cut from low carrier concentration (n or p ~ 10^{14} cm^{-3}) ingots grown by Cominco. The platelets were spring-clamped and thermal-compound greased to a helium dewar copper cold finger having a 3-mm optical aperture. The optical excitation was provided by a stable, CW, grating-tunable CO laser focused onto the sample with a spherical 10-cm focal-length BaF$_2$ lens. The sample was tilted a few degrees from normal incidence to avoid feedback into the CO laser. Forward InSb laser emission was measured directly by a calibrated Eppley thermopile or with a Barnes InSb photovoltaic detector through a Spex 3/4-m grating spectrometer and chopper. The InSb could be probed spatially and wedge-tuned by simple lateral motion of the sample. The magnetic field could be applied in the plane of the platelet normal to the optical propagation.

Thresholds, conversion efficiencies, and spectral properties were measured on a number of samples of varying carrier concentration and type, crystal orientation, and thickness. These variables had little systematic effect on the results except for the thickness dependence of the number of Fabry-Perot modes. The data presented here (except where indicated) are for a Cominco (ingot No. W501) p-type = 4×10^{13} cm^{-3} $\langle 110 \rangle$-face crystal of thickness L = 180 μm operating in a single dominant longitudinal mode.

The CW thresholds of both longitudinal and transverse pumped InSb lasers are compared in Fig. II-3 as a function of the near-resonant incident CO frequency. The threshold of the transverse surface-pumped sample described earlier[1] (Cominco W491-C, n ~ 1.4×10^{14} cm^{-3}, $\langle 111 \rangle$-face, $\langle 110 \rangle$ cleaved edges spaced by 300 μm, thickness ~30 μm) decreases just above the
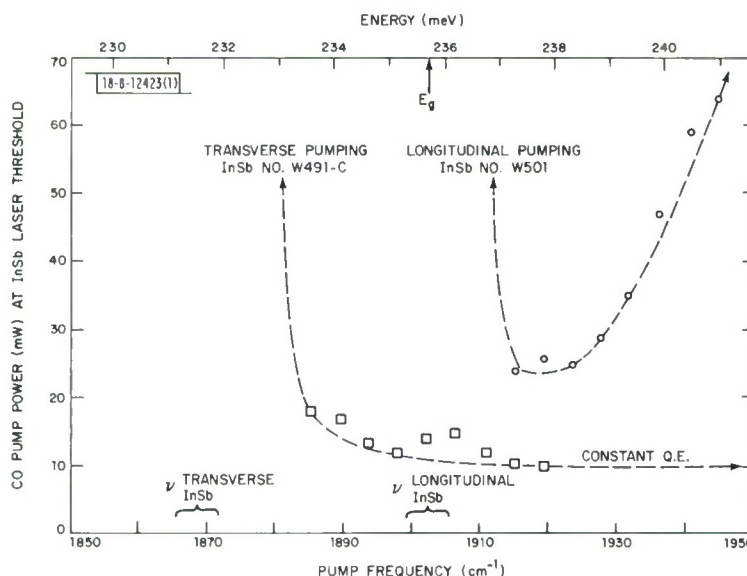
Fig. II-3. Threshold power of InSb laser vs CO pump laser frequency for transverse □ and longitudinal ○ geometry. InSb laser emission range and energy gap indicated.
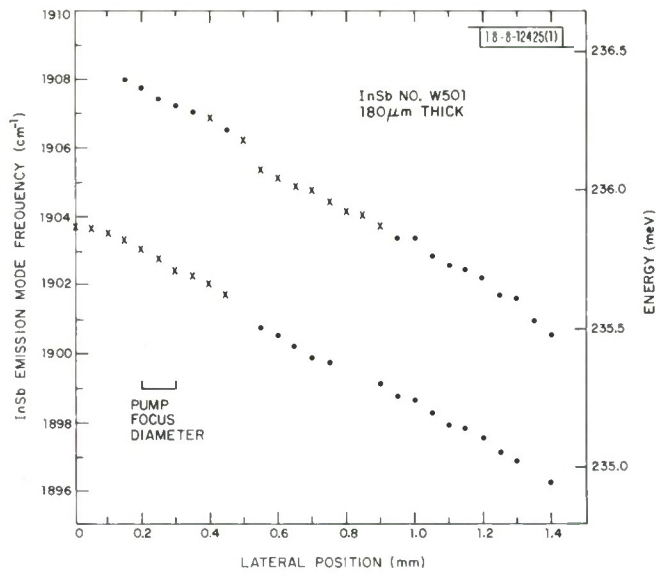
Fig. II-4. Wedge tuning of longitudinal InSb laser modes by lateral displacement. Principal modes indicated by x and subsidiary modes by ●.
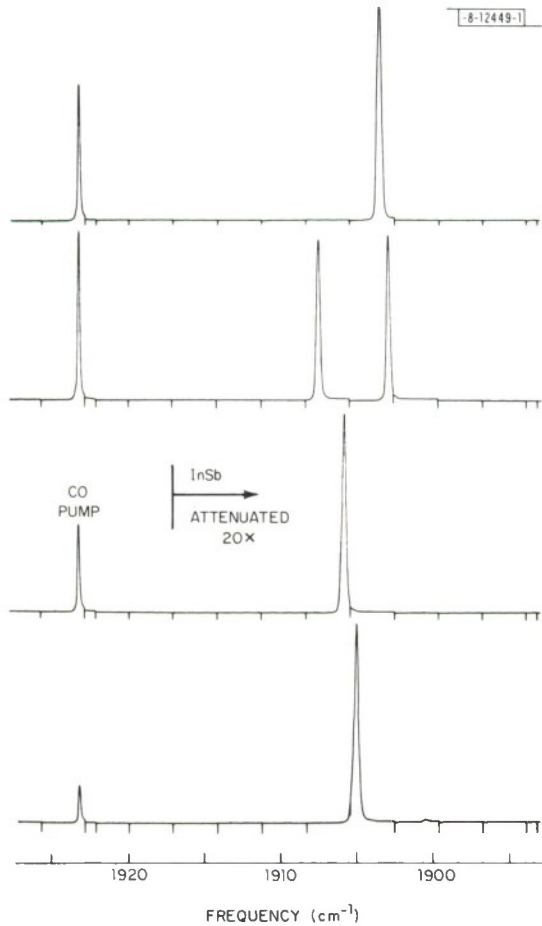
Fig. II-5. Wedge-tuned InSb laser spectra. InSb W 501 corresponding to Fig. II-4. InSb emission is attenuated by a factor of 20 with mica filter to avoid detector saturation for linewidth comparison to residual CO pump line at 1923.5 cm⁻¹.

absorption edge to a shallow minimum, and then increases slowly along a curve of roughly constant quantum efficiency all the way up to a near-1R Nd:YAG pump (65 mW threshold). The threshold of the longitudinal bulk-pumped sample drops precipitously above the absorption edge to a decreasing absorption depth for the higher pump frequency. Continuous longitudinal laser emission could not be achieved with the Nd:YAG laser pump. Also indicated in Fig. II-3 are the range of laser frequencies emitted by the two samples and the published[4] bandgap E_g of the material.

There are several noteworthy points illustrated in Fig. II-3. First, the shapes of the two threshold curves are characteristic of the pumping geometries and are qualitatively explained on the basis of surface and volume excitation. Second, the comparable magnitude of the thresholds at minimum are probably due to the similar excitation volumes and population inversion densities for the two schemes. The transverse pump is focused with a 10-cm cylindrical lens for a beam waist of ~ 100 μm and an excited volume of $\sim 0.9 \times 10^6$ μm^3, assuming carrier diffusion to the rear surface and subsequent confinement. The longitudinally pumped volume is $\sim 2 \times 10^6$ μm^3. The threshold density agreement is fortuitous since thresholds varied by factors of 3 to 5 due to sample inhomogeneity.

The frequency shift exhibited by both the absorption edge and laser emission of the InSb in the two geometries is consistent with a systematic trend toward higher frequencies which has been observed for longitudinally pumped samples in our experiments. The cause of this trend is unexplained.

The longitudinally pumped InSb sample could be mechanically tuned continuously over several cm^{-1} by lateral displacement of the sample, as shown in Fig. II-4. Here, the lack of parallelism of the polished cavity surfaces (~ 0.5 mrad) results in wedge tuning of the Fabry-Perot modes. Principal modes are indicated by crosses, subsidiary modes by dots; a single dominant mode was achieved over much of the range. Some sample inhomogeneity may also contribute to this tuning, particularly where the weaker modes are displaced beyond the original spontaneous gain bandwidth.

Spectral traces of the wedge-tuned InSb laser emission and transmitted CO pump radiation are shown in Fig. II-5. Here, the resolution of the spectrometer (~ 0.1 cm^{-1}) is sufficient to observe a broadening of the InSb mode width over the CO linewidth. This broadening of from 0.1 to 0.3 cm^{-1} is attributed to a number of closely spaced transverse cavity modes associated with each longitudinal mode. The number of transverse modes allowed is roughly $\eta * a^2 / \lambda L$, the Fresnel number, where a is the aperture (or beam) radius. In the case of Figs. II-4 and II-5, $a \sim 50$ μm, $L \sim 180$ μm; so, ~ 13 modes are supportable and are probably launched by the surface roughness and lack of parallelism. The wedge effect over the beam spot size is seen in Fig. II-4 to correspond to the observed width. An investigation of surface roughness in InSb using a 2.5-μm-radius Dektak stylus indicates that surface irregularities are less severe than the wedge effect for causing transverse modes. More refined polishing techniques could sharpen the InSb linewidth, but the Fresnel number still is unfavorably large. A longer cavity decreases the Fresnel number, but increases the possible number of longitudinal modes. Surface aperturing using photoresist etch-roughening could reduce a, but this would eliminate the possibility of wedge tuning or surface probing.

The forward InSb emission corresponding to the spectra of Fig. II-5 was about 7.5 mW in the dominant mode for about 160 mW of incident CO radiation at 1923.5 cm^{-1} and a reflectivity of 44 percent. The double-ended efficiency was therefore ~ 17 percent, which could be increased slightly with magnetic field.
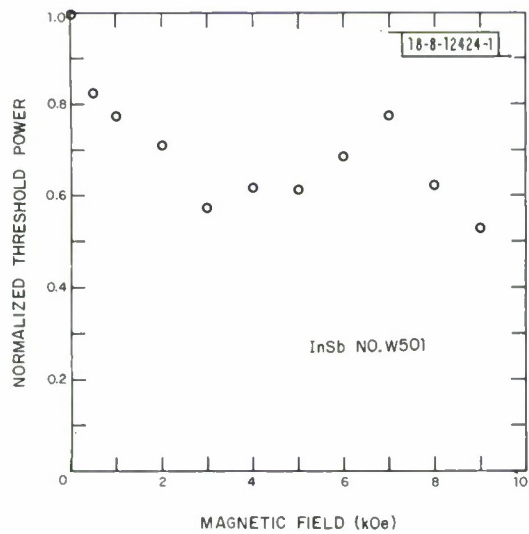
Fig. II-6. Magnetic-field dependence of CW InSb threshold.
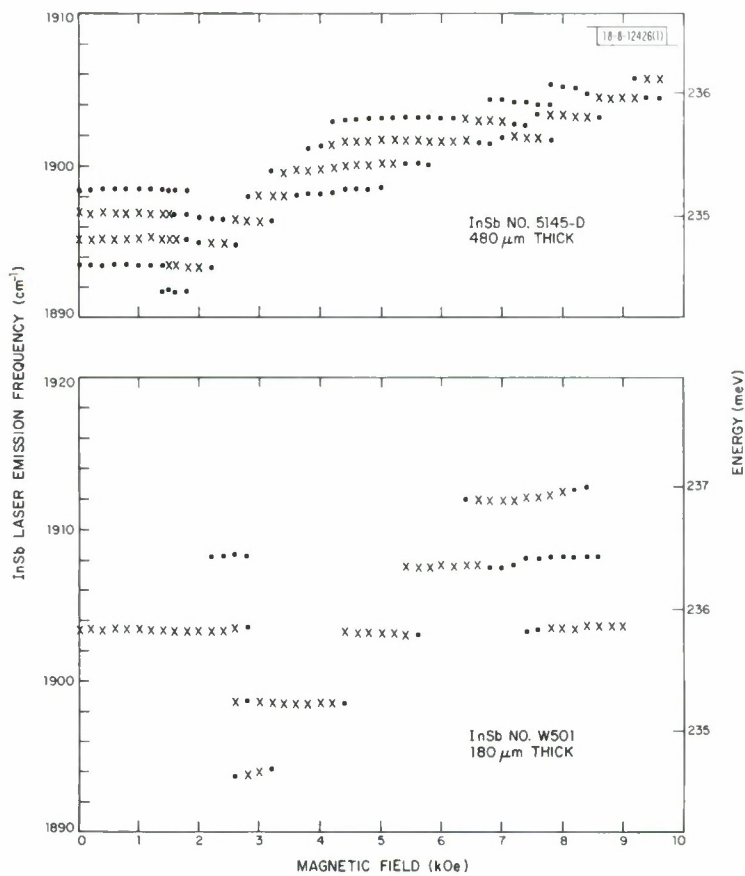
Fig. II-7. Magnetic-field dependence of InSb laser mode frequencies for two sample thicknesses. Principal modes indicated by x and subsidiary modes by •.

2. Magnetic-Field Effects

The magnetic-field dependence of the CW threshold of the longitudinal optically pumped InSb is given in Fig. 11-6. These results resemble previous optically pumped cases,[1,5] and are believed to be due to a field-dependent condensation of the Landau level density of states.[6] This mechanism may explain the Fig. 11-6 threshold variations in correspondence with the mode shifts shown in the lower portion of Fig. 11-7. The double-ended conversion efficiency in this case increases irregularly to ~21 percent at 8.5 kOe with 10-mW forward output for 160-mW pump at 1923.5 cm^{-1} and R = 44 percent.

For CW transverse optically pumped InSb (Ref. 1), a low field (1.5 to 2 kOe) minimum in the emission frequency was observed. Figure 11-7 shows similar results for samples of two different thicknesses optically pumped in a longitudinal geometry. Though there are minor differences in the magnetic-field tuning between these samples and the transverse pumped case, the presence of the low field minimum seems to be independent of pumping geometry, field or crystal orientation, and sample concentration or type. This minimum is believed to be caused by a magnetic-field-induced increase in the binding energy which allows the exciton peak to emerge from the continuum density of states at moderately low fields.[1]

3. Application to Spectroscopy

Doppler-limited spectroscopy at 5.3 μm has been demonstrated with CW InSb lasers optically pumped in the transverse geometry.[1] The longitudinally pumped lasers, with tunable single-mode output of much higher power, have an even greater potential for spectroscopy. At present, the resolution of the device is limited by the broad linewidth (0.1 to 0.3 cm^{-1}) arising from the spurious transverse cavity modes associated with the longitudinal peak. This linewidth, which is barely adequate for atmospheric-broadened spectroscopy, may be improvable with refined fabrication techniques.

The mechanical and magnetic-field tuning techniques are useful to obtain quasi-continuous coverage over tens of cm^{-1}. Mode-hopping is prevalent with magnetic tuning as seen in Fig. 11-7 where each mode pulls very little with field. This behavior is contrary to the InSb spin-flip Raman laser[7] where the extremely sharp spontaneous Raman line magnetically pulls the cavity modes over most of their spacing. In the present case, the broader gain profile and small H-field dependence of η^* results in very small continuous tuning.

Wedge tuning provides potentially continuous coverage between modes as exhibited in Fig. II-4. At present, however, wedge tuning creates annoying amplitude fluctuations due to the stochastic nature of the transverse modes supported by the poorly polished surfaces. For these reasons, mechanical and magnetic-field tuning are most useful for biasing the emission in the spectral range of interest, where temperature tuning can be used for fast, smooth scanning. Such thermal scanning can be achieved simply by modulating the incident pump intensity. An example of real-time temperature tuning is shown in Fig. 11-8 where the CO laser power is 20-percent modulated with a 60-Hz sine wave applied to the discharge voltage. The traces are poorly resolved because the laser linewidth is broader than the spectral features examined.

N. Menyuk
A.S. Pine
A. Mooradian
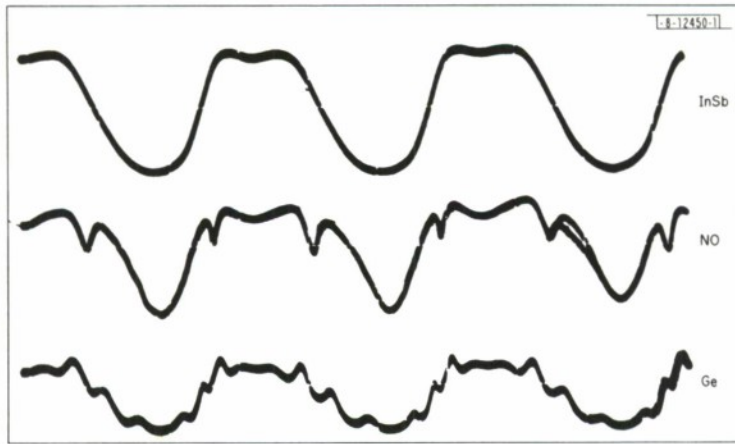
Fig. II-8. Oscilloscope traces of real-time temperature tuning of longitudinal InSb laser by 60-Hz modulation of CO pump intensity. Upper trace: direct frequency and amplitude modulated InSb emission at 1903.1 cm^{-1}. Middle trace: transmission through a 10-cm, 10-Torr cell of NO exhibiting $R_{1/2}(15/2)$ absorption dips upon heating and cooling. Bottom trace: transmission through a Ge etalon with 0.13-cm^{-1} fringe spacing.
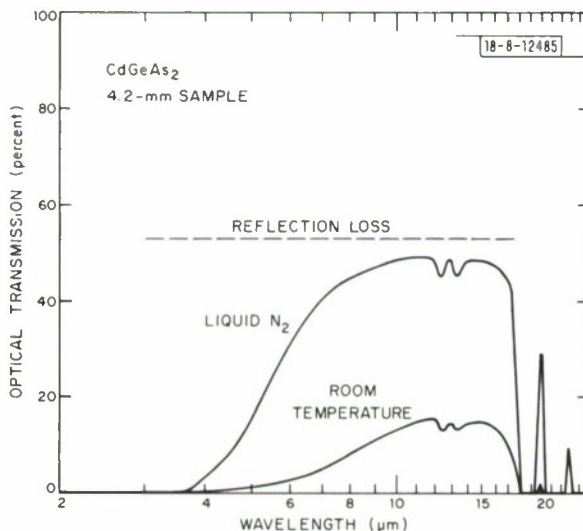
Fig. II-9. Optical transmission through 4.2-mm-thick CdGeAs$_2$ sample.
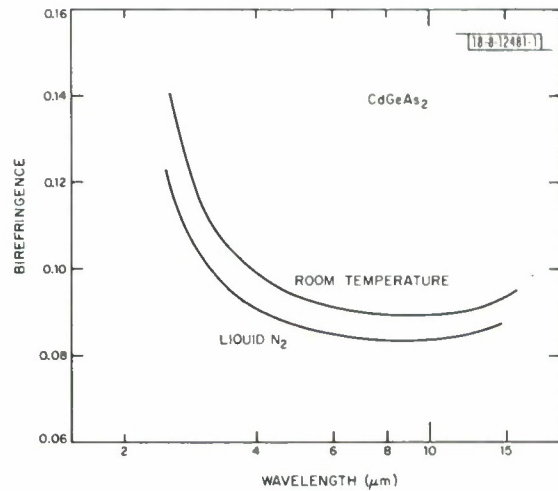
Fig. II-10. Birefringence of CdGeAs$_2$ vs wavelength at room temperature and at liquid nitrogen temperature.

24

C. INFRARED NONLINEAR MATERIALS

1. $CdGeAs_2$

As-grown $CdGeAs_2$ crystals are usually p-type with a room-temperature carrier concentration of 1 to 2×10^{16} cm^{-3}, corresponding to a free-carrier absorption constant of several cm^{-1} in the 5- to 10-μm region.[8] This absorption is too large for nonlinear optical applications. Recently, we have shown that the carrier concentration can be reduced by Li diffusion, although we have not succeeded in eliminating the free-carrier absorption completely. This method, however, is not attractive for larger samples. The free-hole concentration also can be reduced by cooling to liquid nitrogen temperature since $CdGeAs_2$ has deep acceptor levels.[9,10] Figure II-9 shows the improvement in optical transmission for a 4.2-mm-thick $CdGeAs_2$ sample. At liquid nitrogen temperature the transmission losses are low in the 5- to 17-μm region, and there is no evidence of free-carrier absorption. The transmission losses at shorter wavelengths are probably due to scattering and they occur only in p-type samples. Presently, we are investigating how the scattering is affected by changes in the growth conditions.

We have measured the enhancement in the second-harmonic conversion efficiency at liquid nitrogen temperature for the crystal in Fig. II-9 using a CW CO_2 laser operating at 10.59 μm. The crystal, 4.4 mm long, was cut for type 1 phasematching. The phasematching angle changed only slightly with temperature. The total change between room temperature and liquid nitrogen temperature was less than $0.3°$. For 0.4 W of CO_2 power incident on the crystal, the measured second-harmonic power was 0.8 μW at room temperature and at liquid nitrogen temperature it was 14 μW, which is close to what we calculate theoretically for a crystal with no attenuation losses.

We have also tested the crystal as a doubler at liquid nitrogen temperature using a TEA CO_2 laser. With 400 mJ incident on the crystal, we obtained 9 mJ of second-harmonic power corresponding to a conversion efficiency of 2 percent for the uncoated crystal. For comparison, the best doubling result reported for tellurium is less than 1 mJ of second-harmonic power. It is difficult to compare our measured conversion efficiency with theory since the TEA laser did not operate in a TEM_{oo} mode and the output pulse had a nitrogen tail. At the moment, we do not know if the saturation effects observed in room-temperature samples[11] also are present at liquid nitrogen temperature. Concerning the optical damage threshold, our preliminary results indicate that there is no large change between room temperature and liquid nitrogen temperature.

The index of refraction of $CdGeAs_2$ is reduced by approximately 0.05 at liquid nitrogen temperature. Figure II-10 shows the wavelength dependence of the birefringence measured by an interference method using a spectrophotometer with the sample mounted between crossed polarizers.[12] At 10.6 μm, the change in birefringence is approximately 0.006 between room temperature and liquid nitrogen temperature. We can calculate how much this will affect the phasematching angle. For type I phasematching, the phasematching angle is approximately given by[10]

$$\sin \Theta_I \approx \sqrt{D/B} \tag{II-1}$$

where $D = n_o^{2\omega} - n_o^{\omega}$ is the dispersion, and $B = n_e^{\omega} - n_o^{\omega}$ is the birefringence. Differentiation of Eq. (II-1) gives

$$\delta \Theta_I = \frac{1}{2} \tan \Theta_I (\frac{\delta D}{D} - \frac{\delta B}{B}) \quad . \tag{II-2}$$
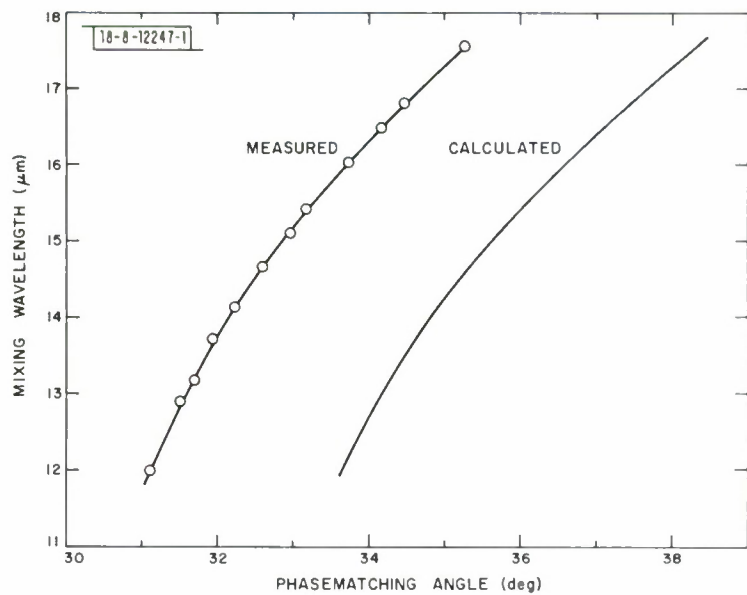
Fig. II-11.   Difference mixing wavelength vs measured and calculated phasematching angles for type I phasematching in $CdGeAs_2$. CO_2 laser is fixed at 9.59 μm, while CO laser is tuned from 5.33 to 6.20 μm.
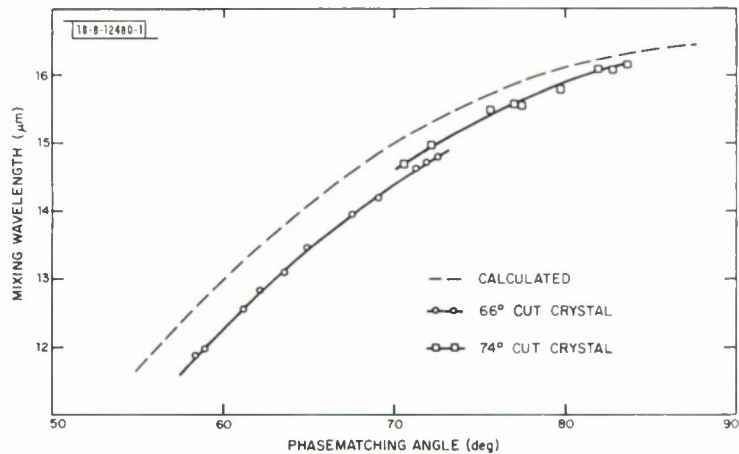
Fig. II-12.   Difference mixing wavelength vs measured and calculated phasematching angles for type I phasematching in $AgGaSe_2$. CO_2 laser is fixed at 9.57 μm, while CO laser is tuned from 5.29 to 6.01 μm.

From this expression, it follows that a change in the birefringence of 0.006 changes the phase-matching angle by 1.2°. This is larger than the measured value; therefore, the change in birefringence must be canceled partially by a change in dispersion.

The type I room-temperature phasematching angles for difference frequency generation of 12- to 17.5-μm radiation have been measured using CW CO and CO_2 lasers. As seen from Fig. II-11, the phasematching angles are about 2° smaller than the value calculated using the Sellmeier expressions. This agrees with previous measurements for type II phasematching.[11]

2. $AgGaSe_2$

Figure II-12 shows the measured type I phasematching angles for difference frequency generation in $AgGaSe_2$. Two crystals were used with the c-axes oriented respectively 66° and 74° to the front surface normal. The measured phasematching angles are approximately 2° larger than the calculated angles from the Sellmeier expressions in Ref. 13, and they change more rapidly with wavelength than for $CdGeAs_2$. To generate between 12 and 16 μm the phasematching angle varies between 59° and 81° for $AgGaSe_2$, while for $CdGeAs_2$ the change is only between 31.1° and 33.7° for type I phasematching.

Figure II-13 shows the measured room-temperature attenuation coefficient between 3.5 and 17.5 μm for a 2.6-cm-thick unannealed $AgGaSe_2$ sample. Most of the transmission losses at short wavelengths are due to scattering, which can be reduced by a combined annealing and
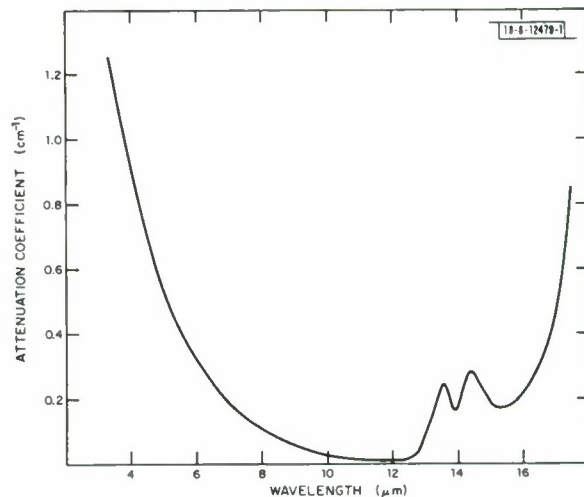
Fig. II-13.   Measured room-temperature attenuation coefficient for 2.6-cm-thick unannealed $AgGaSe_2$ sample.

quenching technique. The best transmission is around 12 μm where the attenuation coefficient is of the order of 0.01 cm^{-1}. Absorption at 13.6 and 14.4 μm is due to three-phonon processes having a magnitude of about 0.2 cm^{-1}. The first two-phonon absorption peak occurs at 20.1 μm and the absorption constant is approximately 60 cm^{-1}. At 16 μm, the room-temperature absorption is about 0.2 cm^{-1}. It should be possible to reduce this by cooling to liquid nitrogen or helium temperature since the phonon bands sharpen up.

H. Kildal
G.W. Iseler

D.   SPIN-FLIP SCATTERING LINESHAPE STUDIES

The measurements of the spontaneous spin-flip Raman linewidth reported previously[14] have been extended into the high-magnetic-field, high-carrier-concentration regime. This is the
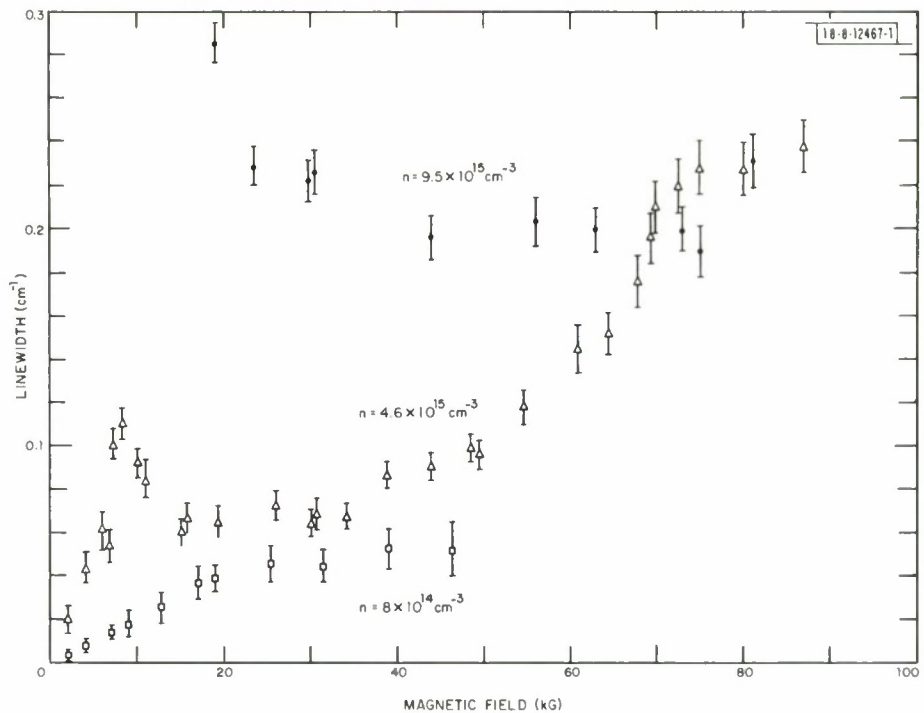
Fig. II-14. Linewidth of forward spin-flip Raman scattering (T ~ 2 K).

operating parameter regime of the high-energy spin-flip laser described in Sec. E below. These measurements represent a substantial increase in resolution over available results for samples in this magnetic field and electron concentration range.[15]

The linewidth results as a function of magnetic field for samples in the concentration range from $n = 8 \times 10^{14}$ to 1×10^{16} cm^{-3} are shown in Fig. II-14. The linewidth was measured in the forward-scattering geometry with both photons propagating normal to the magnetic field. These data were taken with the samples immersed in superfluid helium at T ~ 2 K. For a carrier concentration of $n = 9.5 \times 10^{15}$ cm^{-3}, the spin-flip linewidth is almost invariant at 0.2 cm^{-1} for magnetic fields greater than about 25 kG. This field corresponds to the quantum limit field above which all the electrons are in the lowest spin level. For this regime, a previous theoretical linewidth calculation[15,16] has given the linewidth dependence

$$\Gamma \sim 2 \left| \frac{1}{\tau_s} + \tau_p \left[\langle (\omega_s - \langle \omega_s \rangle)^2 \rangle \, \right] \right| \tag{II-3}$$

where τ_s is the spin relaxation time, τ_p is a momentum relaxation time, and $\langle \omega_s \rangle$ denotes the value of the spin frequency averaged over the electronic momentum distribution. The spin frequency is dependent on the electron momentum because of nonparabolicity effects introduced by the InSb bandstructure. To lowest order, this dependence is given by

$$\omega_s = \omega_{so}(1 - 2 \, \epsilon / \epsilon_g) \tag{II-4}$$

where ω_{so} is the spin frequency at the bottom of the band, $\epsilon = h^2 k_z^2 / 2m_c$ is the kinetic energy corresponding to the electron momentum, and ϵ_g is the bandgap energy. In the limits of degenerate and nondegenerate statistics, Eq. (II-3) can be readily evaluated to give $\Gamma \sim 2/\tau_s + (32/45) \, \tau_p \omega_{so}^2 \epsilon_F^2 / \epsilon_g^2$ for degenerate statistics, with ϵ_F the Fermi energy and

$\Gamma \sim 2/\tau_s + 2\tau_p \omega_{so}^2 (kT_e)^2/\epsilon_g^2$ for nondegenerate statistics. The magnetic-field dependences of these two expressions are quite different; for constant τ's, $\Gamma \propto a + b/H^2$ for degenerate statistics due to the $1/H^2$ dependence of ϵ_F in the quantum limit, while for nondegenerate statistics $\Gamma \propto a + b'H^2$.

For the highest electron concentration measured, the sample is degenerate for most of the magnetic-field range and the linewidth does decrease with increasing magnetic field as predicted. The increase at the higher magnetic fields is probably due to increasing thermal effects [$\epsilon_F/kT_e \sim$ 1 for H = 80 kG and T_e = 6 K (see Ref. 17)]. For the $n = 5 \times 10^{15}$ cm^{-3} sample, the electron gas is nondegenerate over most of the magnetic-field range ($\epsilon_F/kT_e \sim$ 1 for H = 38 kG and T_e = 6 K), and therefore the linewidth increases almost quadratically with magnetic field. The structure in the linewidth dependence at fields below 11 kG is probably associated with the transition to the quantum limit, which occurs at 15 kG for this electron concentration. For a τ_p of 5×10^{-13} sec, which is of the order of magnitude of the τ_p needed to fit linewidth data on comparably doped samples in the geometry in which the scattered light is collected along the magnetic field,[15] an electron temperature of 6 K provides a good fit to the data. This temperature rise above the 2 K lattice temperature under the laser excitation is not unreasonable.

The data for the 8×10^{14} cm^{-3} sample do not show the expected H^2 dependence, but these linewidths are probably dominated by spin relaxation effects (e.g., τ_s) since the calculated non-parabolicity contributions to the linewidth are smaller than the observed linewidths. Data were not taken at higher fields due to the reduction in signal for this low concentration sample as the resonance enhancement of the gain decreased.[15]

In summary, the spontaneous spin-flip Raman scattering linewidth has been measured for electron concentrations in the range 10^{15} to 10^{16} cm^{-3}, and magnetic fields from 2 to 80 kG. These parameter values span the practical range (with the exception of still higher concentrations) for obtaining high-energy spin-flip laser operation in the 11- to 12-μm region. Qualitative agreement between theory and experiment is found for the magnetic-field and carrier-concentration dependences of these linewidths. These results are useful in evaluating some of the trade-offs, such as between output power and spectral width, that must be made in designing a spin-flip laser for a specific application.

<div align="right">S. R. J. Brueck</div>

E. HIGH-OUTPUT-ENERGY SPIN-FLIP LASER

A high-output-energy (600 μJ single-ended), 11- to 12-μm InSb spin-flip laser system using a CO_2 TEA laser pump has been constructed, and preliminary results on output energy and spectral characteristics have been obtained. The TEA laser source used initially in these experiments was a helical resistive pin design which gave a 200-mJ multi-transverse mode output pulse on the P(20) line of the 10.6-μm band of CO_2 at 945 cm^{-1}. The $1 \times 1 \times 1.5$ cm^3 InSb spin-flip crystal which was immersed in superfluid liquid helium was mounted in the bore of a superconducting magnet. The incident pump beam, collimated to a beam waist of approximately 0.4-cm diameter by BaF_2 lenses, was directed perpendicular to the magnetic field in the long dimension of the sample and polarized along the magnetic field. This geometry has been theoretically predicted[18] to have lower threshold and saturation powers than the geometry with the incident beam polarized perpendicular to the magnetic field. The InSb electron concentration
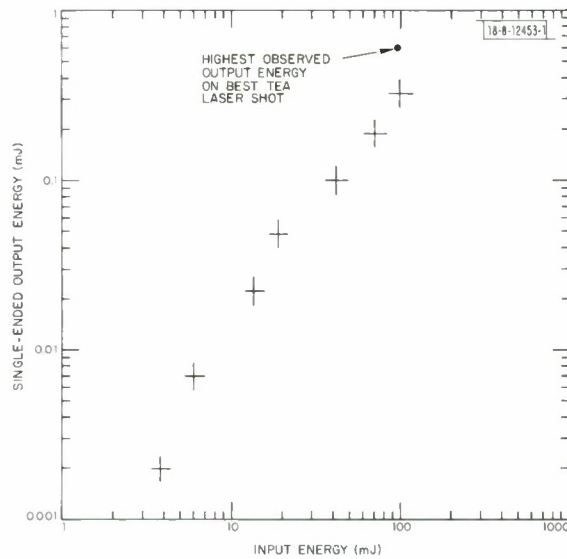
Fig. II-15. Input-output energy dependence of 10.6-μm spin-flip laser (n = 1 $\times$ 10^{16} cm^{-3}, ℓ = 1.5 cm, T = 2 K, input pulse-width ~ 2 μsec, H = 45 kG).
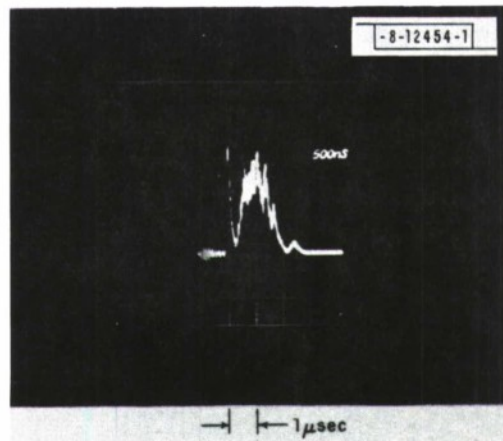
Fig. II-16. Spin-flip laser output pulse (n = 1 $\times$ 10^{16} cm^{-3}, ℓ = 1.5 cm, T = 2 K, input pulsewidth ~ 2 μsec, H = 45 kG).

specified by the supplier was n ~ 1.0 $\times$ 10^{16} cm^{-3}. At H = 30 kG, the spontaneous spin-flip linewidth (see Sec. D above) measured on this sample was 0.16 cm^{-1}, indicating that the actual concentration was somewhat below 10^{16} cm^{-3}.

The input-output energy characteristics for this sample at a magnetic field of 45 kG (λ = 11.7 μm) are shown in Fig. II-15. These data have been referred to the energies just outside the spin-flip crystal; that is, window and filter transmission losses have been corrected for. Note that while the slope is lower at the higher input energies, saturation has not been reached. Due to apparent damage problems on the Irtran cold windows, higher pump-power densities were not used. Peak single-ended spin-flip output energies of 0.6 mJ were obtained from this crystal. At a magnetic field of 60 kG, λ = 12.1 μm, the peak output energies were reduced by about a factor of 2 from those at 45 kG.

The spin-flip output pulse shape at H = 45 kG and the 0.5-mJ energy level are shown in Fig. II-16. There is a short (100-nsec) leading spike followed by a turn off lasting approximately 300 nsec, and then a long pulse of 1.5-μsec duration which contains most of the spin-flip laser energy. The spin-flip laser output level did not decrease completely to zero after the initial pulse but remained at some low level. The input CO_2 pulse had a leading gain-switched peak of about 250-nsec duration and a tail extending out 1.5 μsec which contained approximately 75 percent of the pulse energy. The magnitude of the gain-switched peak relative to the tail intensity was reduced when the beam was transmitted through the InSb sample, indicating that some two-photon or other nonlinear processes were occurring in the sample. The transmitted CO_2 beam showed a relatively smooth intensity profile in time without any indication of the initial sharp spike followed by a decrease in intensity of the spin-flip output. The thresholding behavior of the two components of the spin-flip output was quite different. At low pump energies, up to about 12 mJ only the sharp spike was observed. Above this energy, the broad second pulse appeared and increased rapidly in peak intensity to become comparable to the initial spike intensity.

The spectral characteristics of the spin-flip laser output at this high-energy level were investigated with a flat-flat Fabry-Perot interferometer. The results of a series of traces with a 1-cm mirror spacing (0.5-cm^{-1} free spectral range) are shown in Fig. II-17 where trace (a) shows a scan of the CO_2 pump laser radiation transmitted through the sample. A scan of the spin-flip output at the 0.5-mJ output level is shown in trace (b). Note that the spin-flip output is close to single longitudinal mode and has a (resolution-limited) linewidth of less than 0.07 cm^{-1}. If the pump laser spot on the sample was misaligned, the spin-flip laser could be forced to lase with a multi-transverse mode structure in what was probably a bounce-mode operation [trace (c)]. In practice, misalignment means having the input pump beam near an edge of the InSb sample. The spacing between these modes was about 0.07 cm^{-1}, in reasonably good agreement with the 0.08-cm^{-1} mode spacing calculated from the sample length. The width of each mode was again approximately 0.07 cm^{-1}, and the total spectral extent was about 0.25 cm^{-1}. Also,
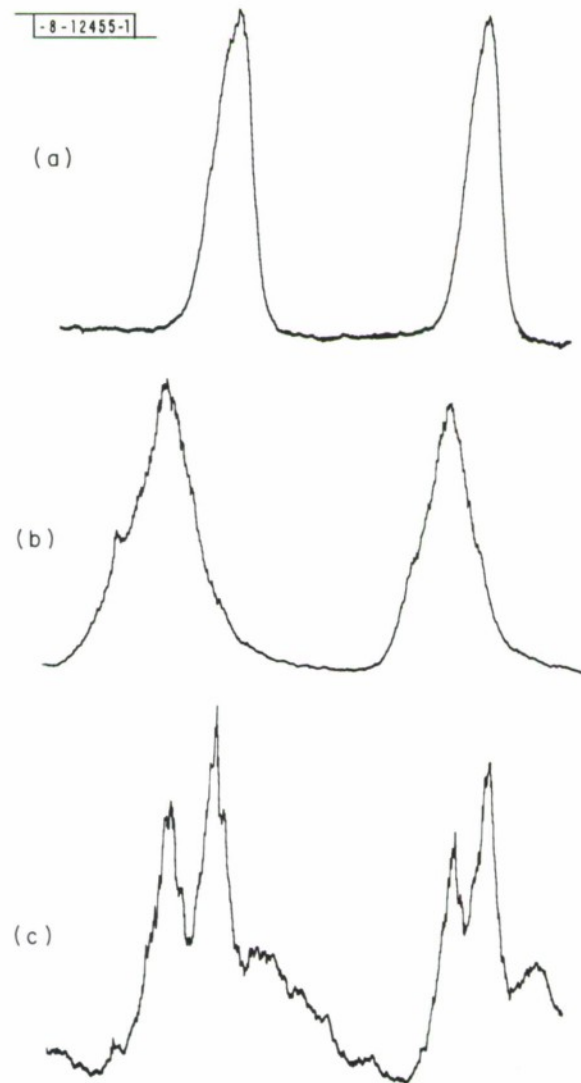
Fig. II-17. Fabry-Perot traces of spin-flip and pump laser outputs: (a) CO_2 pump laser output, (b) single-mode spin-flip laser output, (c) multi-longitudinal bounce-mode spin-flip laser output.

the total output pulse energy in this multimode case was considerably lower than that observed for the much cleaner output pulses of trace (b).

As the magnetic field was varied, the single mode output of trace (b) in Fig. II-17 tuned smoothly (within the instrument resolution) with a tuning rate of about 18 MHz/G over a range of almost 400 G (0.23 cm^{-1}), and then mode jumped about 0.5 cm^{-1}. These tuning character- istics are somewhat surprising since the longitudinal mode spacing is only 0.08 cm^{-1}, which would seem to require more frequent mode jumps than are observed. In addition, the cavity Q is much lower in this 10-μm regime than at 5 μm, and this would imply that the mode tuning rates should be higher at 10 μm than those observed[7] at 5 μm for comparably doped samples.

A double-discharge TEA laser has recently been assembled to investigate the output char- acteristics of the spin-flip laser under a variety of different pulse shape excitations.[19] Pre- liminary results with a short 200-nsec TEA laser pulse (no N_2 in laser gas mixture) indicate very different characteristics than those reported above. The spin-flip output energy level rises much more rapidly near threshold than in Fig. II-15 and abruptly saturates at an input power level of about 10 mJ.

These output characteristics are consistent with the results reported by other workers (cf. Ref. 18) and indicate that the characteristics reported above are associated with the presence of the long tail on the input TEA laser pulse. The long time scale of the output characteristics indicates that the effect is probably not a transient phenomena but is associated with a steady- state decrease in the spin-flip output level under high excitation levels. This probably is due to the effects of free-carrier absorption in the electronic-distribution function. This mechanism is presently being investigated in more detail.

S. R. J. Brueck
A. Mooradian

REFERENCES

1. A. S. Pine and N. Menyuk, Appl. Phys. Lett. 26, 231 (1975); Solid State Research Report, Lincoln Laboratory, M.I.T. (1974:4), p. 31, DDC AD-A004763.

2. G. E. Stillman, M. D. Sirkis, J. A. Rossi, M. R. Johnson and N. Holonyak, Appl. Phys. Lett. 9, 268 (1966).

3. M. R. Johnson and N. Holonyak, J. Appl. Phys. 39, 3977 (1968).

4. S. Zwerdling, W. H. Kleiner and J. P. Theriault, J. Appl. Phys. 32S, 2118 (1961).

5. R. J. Phelan, Jr., Physics of Quantum Electronics, edited by P. L. Kelley, B. Lax and P. E. Tannenwald (McGraw-Hill, New York, 1966), p. 435.

6. A. P. Shotov, M. S. Mirgalovskaya, R. A. Muminov and M. R. Raukhman, Sov. Phys.-Semicond. 1, 1193 (1967).

7. S. R. J. Brueck and A. Mooradian, Appl. Phys. Lett. 18, 229 (1971), DDC AD-729611.

8. H. Kildal, Phys. Rev. B 10, 5082 (1974).

9. A. A. Vaipolin, F. M. Gashimzade, N. A. Goryunova, F. P. Kesamanly, D. N. Nasledov, E. O. Osmanov and Yu. V. Rud, Academy of Sciences of the U. S. S. R., Bull. Phys. Series 28, 984 (1964).

10. H. Kildal, Air Force Materials Laboratory Technical Report AFML-TR-72-277, Air Force Systems Command, Wright-Patterson Air Force Base, Ohio (December 1972).

11. H. Kildal and J. C. Mikkelsen, Opt. Commun. 10, 306 (1974), DDC AD-A000516/5.

12. S. A. Abagyan, G. A. Ivanov, A. A. Kartushina and G. A. Koroleva, Sov. Phys.-Semicond. 5, 1425 (1972).

13. H. Kildal and J. C. Mikkelsen, Opt. Commun. 9, 315 (1973), DDC AD-777560/4.

14. Solid State Research Report, Lincoln Laboratory, M.I.T. (1974:3), p. 19, DDC AD-A001595/8.

15. S. R. J. Brueck and F. A. Blum, Phys. Rev. Lett. 28, 1458 (1972), DDC AD-752954; S. R. J. Brueck, A. Mooradian and F. A. Blum, Phys. Rev. B 7, 5253 (1973), DDC AD-772151/7.

16. S. R. J. Brueck and A. Mooradian, Opt. Commun. 8, 263 (1973), DDC AD-772118/6.

17. Electron temperatures T_e under the laser excitation are elevated somewhat above the lattice temperature; see, for example, A. Mooradian, S. R. J. Brueck, E. J. Johnson and J. A. Rossi, Appl. Phys. Lett. 21, 482 (1972), DDC AD-753311.

18. M. H. Weiler, R. L. Aggarwal and B. Lax in Proceedings of the 12th International Conference on the Physics of Semiconductors, M. H. Pilkuhn, Ed. (B. G. Teubner, Stuttgart, 1974), p. 798.

19. A. Girard and A. J. Beaulieu, IEEE J. Quantum Electron. QE-10, 521 (1974).

III. MATERIALS RESEARCH

A. PHOTOELECTROLYSIS OF WATER

Although the free energy required for the decomposition of water into gaseous H_2 and O_2 is only 1.23 eV, while the peak of the solar spectrum occurs at a photon energy of about 2.4 eV, solar energy cannot be utilized for the production of H_2 fuel by the direct photodecomposition of water because the threshold energy for this reaction is about 6.5 eV. However, the photon energy threshold can be reduced greatly if decomposition is accomplished by means of photoelectrolysis, a process in which a semiconductor is used as a catalyst.[1] As reported earlier,[2] in order to evaluate the potential of photoelectrolysis as a means for the large-scale utilization of solar energy we are investigating its physics and electrochemistry by experiments on cells consisting of an n-type TiO_2 anode, an aqueous electrolyte, and a Pt cathode. We now have succeeded in obtaining external quantum efficiencies as high as 80 to 85 percent, corresponding to internal quantum efficiencies close to 100 percent, for cells that have been optimized with respect to the ratio of cathode and anode areas and to the pH of the electrolyte.

In a photoelectrolysis cell, because of the difference between the work functions of the semiconducting TiO_2 and the electrolyte, the TiO_2 energy bands are bent at the surface, so that the analog of a Schottky barrier exists at the semiconductor-electrolyte interface. (See the energy diagram in Fig. IV-6 of Ref. 2.) When the TiO_2 is irradiated by photons of energy at least equal to its energy gap, 3.0 eV, the hole-electron pairs generated at its surface by photon absorption do not recombine but are separated by the electric field of the barrier; the electrons move away from the surface into the bulk of the TiO_2 and then through the external circuit to the Pt cathode where they discharge $H_2(2e^- + 2H^+ \rightarrow H_2)$, while the holes remain at the surface where they can interact with the electrolyte to produce $O_2(2p^+ + H_2O \rightarrow 0.5\ O_2 + 2H^+)$. The overall chemical reaction is

$$2h\nu + H_2O \rightarrow 0.5\ O_2 + H_2 \qquad\qquad (III-1)$$

since TiO_2 is chemically inert in aqueous solution (unlike many other n-type semiconductors, which exhibit anodic dissolution), serving only to absorb the light and to produce the holes and electrons that make the reaction possible. We have measured the band bending in TiO_2 as a function of electrolyte pH by using both the differential space-charge capacitance and surface photovoltage techniques[3] to determine the flat-band potential. This is the potential of the semiconductor electrode (with respect to a reference electrode — in our case the saturated calomel electrode) at which the bands are not bent. With increasing pH, the flat-band potential was found to vary linearly with a slope of 0.059 eV/pH (i.e., 2.303 e/kT), as expected if the principal effect of the change in pH is to vary the Fermi level in the solution.[4]

Since the band bending in TiO_2 increases with pH, we expected that the efficiency of photoelectrolysis would also increase with pH. To check this prediction, the operating characteristics of photoelectrolytic cells under constant illumination from a 150-W Xe source were measured for various values of pH. Typical results, obtained for pH = 0, are plotted in Fig. III-1. The upper curve gives the output voltage V as a function of the current drawn from the cell per cm^2 of illuminated TiO_2 surface. The lower curve gives the electrical power P extracted by the load. For maximum photoelectrolysis, the cell is operated in the short-circuit mode; for this

35
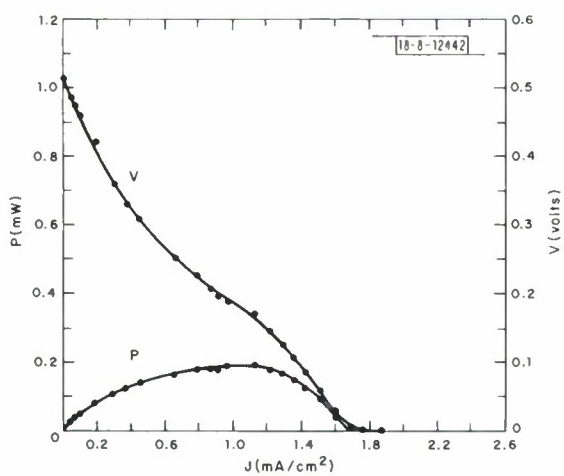
Fig. III-1. Operating characteristics of TiO_2/Pt photoelectrolysis cell at pH = 0. Output voltage V and power to external load P are plotted against current density J.
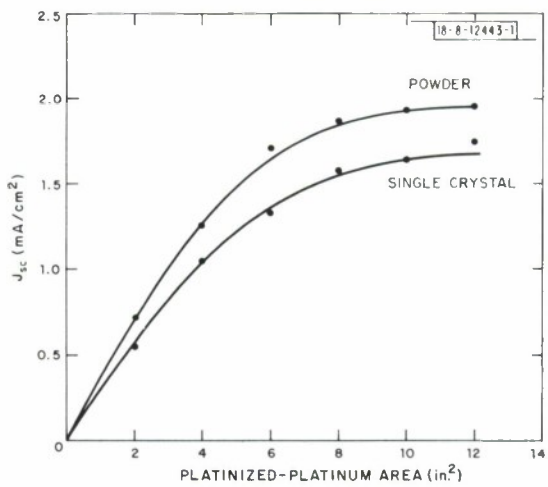
Fig. III-2. Short-circuit current density (J_{sc}) as a function of cathode area for photoelectrolysis cell at pH = 0. Area of TiO_2 anode was 1 cm^2.
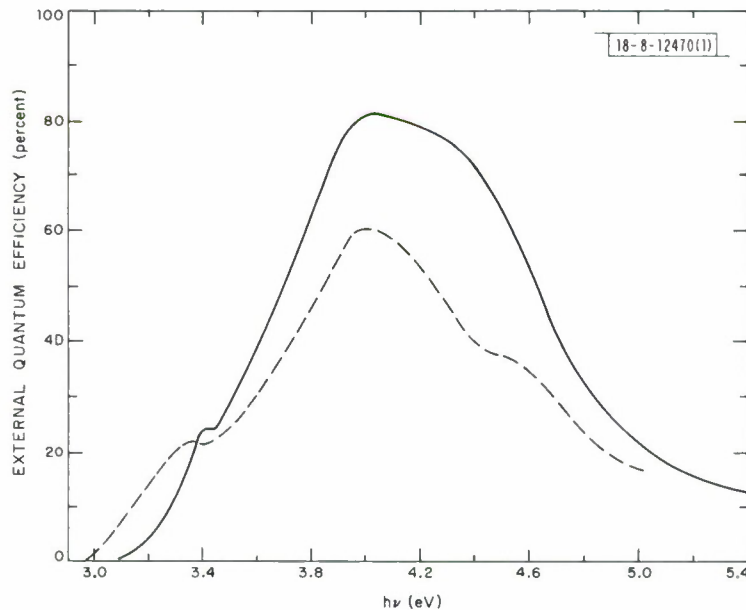
Fig. III-3. Variation of external quantum efficiency with photon energy (hν) for photoelectrolysis cell with single-crystal (solid line) or hot-pressed (dashed line) TiO_2 anode.

example, the current density J_{sc} = 1.88 mA/cm^2. If the cell is operated at $J < J_{sc}$, electrical power can be extracted at the same time as gas is discharged. The two curves in Fig. III-1 can be fit to a fairly good approximation by a model that considers the photoelectrolysis cell as a constant voltage source in series with an internal resistance. Here, the open-circuit voltage is 0.52 V and the internal resistance is ~350 Ω.

Measurements of J_{sc} vs pH made on our initial cell, which had a platinized-platinum cathode area about 13 times greater than the TiO$_2$ surface area, yielded the unexpected result that J_{sc} was a maximum at pH = 0, where the band bending is the smallest. Since pH = 0 corresponds to a maximum concentration of H$^+$ ions, this observation suggested that the discharge of H$^+$ ions at the cathode was the rate-limiting step in the cell. This was confirmed by measurements of J_{sc} at pH = 0 as a function of the geometric cathode area, which showed (Fig. III-2) that J_{sc} increased until the ratio of cathode-to-anode area was about 50. When the J_{sc}-vs-pH measurements were repeated on a cell with this area ratio, the predicted increase in J_{sc} was observed until the pH reached 4.7, after which the current became essentially constant. Thus, such an optimized cell (in which the evolution of O$_2$ is the rate-determining step) can operate with maximum efficiency with a neutral electrolyte, i.e., at a pH of ~7.

To determine whether the rate of O$_2$ evolution was limited by the rate of hole generation, we also investigated the variation of the short-circuit current with light intensity. The curve of J_{sc} vs light intensity (with photons at hν ~ 4 eV, which as discussed below is the energy of peak response of the cell) is linear at low intensity, but bends over at intensities higher than about 5 mW/cm^2. On a clear day, the intensity of solar radiation within the 3- to 4-eV spectral region is between 2 and 4 mW/cm^2, which is in the linear-response region of the cell.

The external quantum efficiency η as a function of photon energy hν was measured on an optimized photoelectrolytic cell for light intensities in the linear region. The anode was illuminated by monochromatic light from a source consisting of a 1000-W Xe lamp and a grating monochromator. The light intensity S incident on the cell was measured as a function of hν by means of a thermopile power meter that had a flat response down to 0.25 μm. The value of η, defined as the ratio of the number of electrons flowing in the external circuit (N_e) to the number of photons incident on the cell (N_p), was calculated at each value of hν from

$$\eta = \frac{N_e}{N_p} = \frac{J_{sc}(A/cm^2)/e(C)}{S(W/cm^2)/[h\nu(eV) \times e(C)]} = \frac{J_{sc}}{S} h\nu \quad . \tag{III-2}$$

Figure III-3 shows the values of η vs hν for a single crystal and a hot-pressed disk (both measured in a buffered electrolyte with pH = 8). The maximum values of η, 82 percent for the single crystal and 60 percent for the polycrystalline disk, occur at h$\nu \approx$ 4 eV. The highest values of η previously reported[1] for photoelectrolysis without electrode decomposition have been about 10 percent.

Quantum efficiency measurements also were made with TiO$_2$ films on Ti foil that had been thermally oxidized. The results for two such films, prepared under different conditions and measured in a nonbuffered electrolyte of pH 13, are shown in Fig. III-4. For film A (7 μm thick), η reaches a maximum value of 84 percent at λ = 3400 Å (~3.5 eV), while film B (<2 μm thick) has a maximum of 83 percent at 3000 Å (~4 eV). The positions of the quantum efficiency peaks in Figs. III-3 and III-4 correspond to major absorption peaks in TiO$_2$ that occur at about 3.5, 4, and 4.7 eV (3400, 3000, and 2600 Å), respectively.[5] The relative intensities of the efficiency peaks depend on preparation procedure and oxide layer thickness.
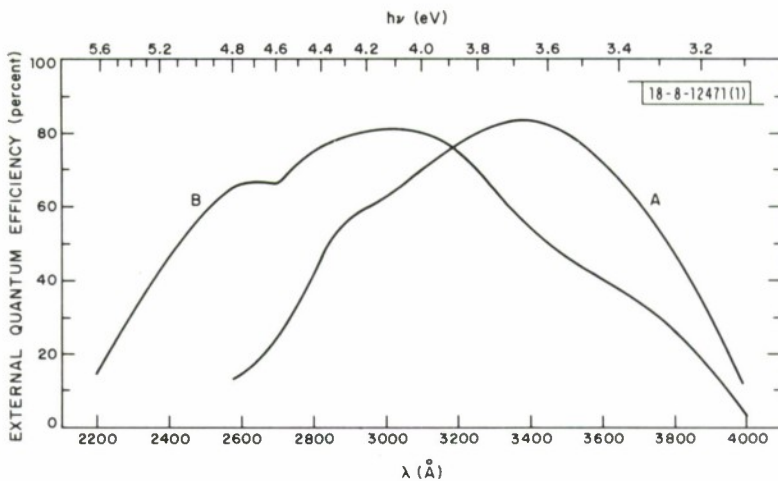
Fig. III-4. Variation of external quantum efficiency with wavelength λ for photoelectrolysis cell with two different anodes prepared by thermal oxidation of Ti foil.

When the maximum η values are corrected by taking account of estimated reflection losses at the interfaces and absorption losses in the electrolyte, we find that the internal quantum efficiency is close to 100 percent. This high quantum efficiency shows photoelectrolysis to be a very promising method for the direct conversion of solar energy to chemical energy in the form of gaseous H_2, a fuel that can be stored indefinitely and transported conveniently over long distances. In spite of the mismatch between the solar spectrum and the spectral response of TiO_2 cells, illumination of our optimized cells with sunlight has yielded efficiencies as high as 1 percent for the conversion of solar energy into chemical energy. This is to be compared with ~15-percent solar conversion efficiency for electrical energy generation by the best single-crystal Si photovoltaic cells, and ~5-percent efficiency for polycrystalline photovoltaic cells.

Improved conversion efficiencies for utilization of solar energy by photoelectrolysis could be achieved by finding a satisfactory anode material with a lower energy gap than TiO_2, since only about 10 percent of the energy in solar radiation reaching the earth is above the threshold of 3.0 eV observed for photoelectrolysis with TiO_2. Furthermore, a larger portion of the sun's energy spectrum could be utilized by using a combination of suitable semiconductor electrodes.

<div style="text-align: right">

J. G. Mavroides   D. F. Kolesar
D. I. Tchernev   W. J. LaFleur
J. A. Kafalas   D. M. Tracy

</div>

B. ELECTRONIC STRUCTURE OF TiO_2 AND Ti_2O_3 SURFACES

In an attempt to elucidate the catalytic behavior of transition-metal oxides, we have undertaken a study of the electronic properties of their surfaces. Our initial work has been on the oxides of titanium because TiO_2 is used as the catalytic electrode in the decomposition of H_2O by photoelectrolysis, a process currently being investigated in the Laboratory (see Sec. III-A).

To date, we have employed electron energy-loss spectroscopy (ELS) as our main experimental method in this study because of its extreme sensitivity to surface properties. In ELS, the sample is bombarded with a beam of monoenergetic electrons, and the energy distribution of the electrons emitted from the sample is analyzed. The region of the secondary-electron spectrum

immediately below the elastically reflected peak at the incident-electron energy E_I consists mainly of electrons that have excited a transition of energy Δ in the sample and emerged with an energy $(E_I - \Delta)$. The surface sensitivity of ELS is due to the very short mean-free-paths of low-energy electrons in solids (3 to 10 Å for $20 \leqslant E \leqslant 500$ cV). For the measurements reported here, E_I was 30 eV, and the energy-loss spectra were measured with a single-pass cylindrical-mirror analyzer. The resolution of the measurements was about 0.8 eV.

Samples of TiO_2 and Ti_2O_3 were cut from single-crystal boules. To obtain fresh surfaccs, they were broken (we were unable to cleave them) immediately prior to mounting in the ultrahigh-vacuum system. Whether the samples were broken in air or in a glove bag under N_2 gas made no difference in their spectra. Freshly broken TiO_2 surfaces produced a few faint LEED spots, indicating some degree of atomic ordering of the surface. Only one broken Ti_2O_3 surface showed any LEED spots, and they were very faint.

Energy-loss spectra for TiO_2 and Ti_2O_3 samples are shown on the left and right sides, respectively, of Fig. III-5(a-d) where the derivative $dn(E)/dE$ is plotted against the energy loss, $E_L \equiv E_I - E$, so midpoints of negative slopes correspond to peaks in $n(E)$ vs E_L. For freshly
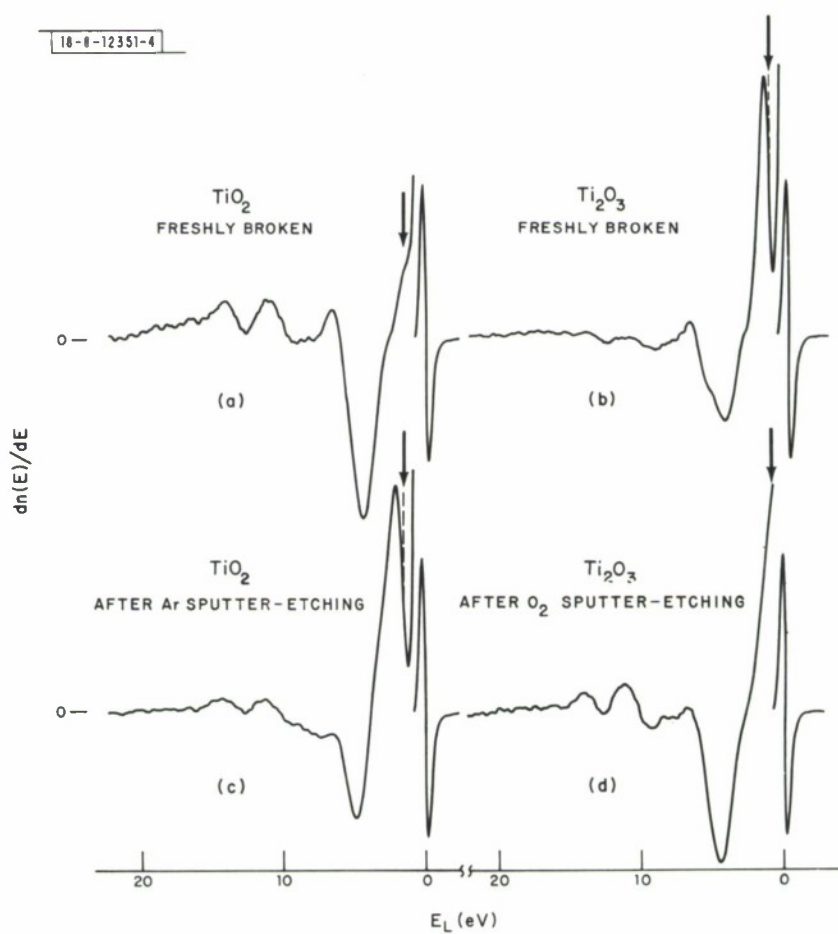
Fig. III-5. Electron energy-loss spectra, $dn(E)/dE$ vs E_L, for (a) freshly broken TiO_2, (b) freshly broken Ti_2O_3, (c) Ar-ion sputtcr-etched TiO_2, and (d) O-ion sputter-etched Ti_2O_3. Arrows indicate $E_L = 1.5$ eV. Incident-beam energy was 30 eV.
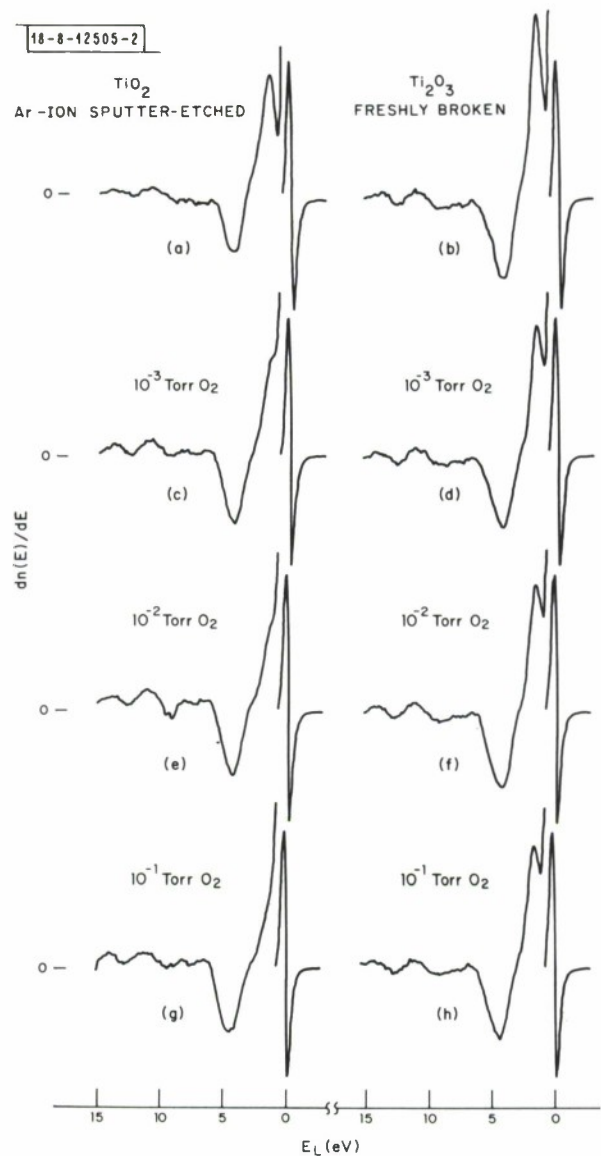
Fig. III-6. Electron energy-loss spectra, dn(E)/dE vs E_L, for TiO_2 and TiO_3, both before [(a) and (b)] and after [(c) through (h)] exposure for 10 minutes to O_2 at pressures specified. Incident-beam energy was 30 eV.

broken TiO_2 [Fig. III-5(a)], peaks in n(E) occur at energies of 5.5, 10.0, and 13.5 eV. The same three peaks occur for freshly broken Ti_2O_3 [Fig. III-5(b)], but with slightly different relative amplitudes. The major difference between the two spectra is that at E_L = 1.5 eV (indicated by the arrows), a large peak is observed for Ti_2O_3 but not for TiO_2.

We have found that the energy-loss spectra of these surfaces can be changed reversibly by sputter-etching with inert gases or oxygen. The spectrum for TiO_2 after sputter-etching with 500-eV Ar ions [Fig. III-5(c)] shows a strong peak at 1.5 eV and is very similar to that for freshly broken Ti_2O_3 [Fig. III-5(b)], suggesting that the surface has been reduced by the ion bombardment. This is confirmed by a comparison between the Auger-electron spectra for the two TiO_2 surfaces, since sputter-etching is found to decrease the ratio of the O to Ti Auger peaks by 5 percent. (Because the Auger electrons sample a greater depth of the crystal than do the ELS electrons, the two experiments cannot be compared quantitatively.) Furthermore, the surface of Ti_2O_3 can be oxidized by sputter-etching with O ions, as shown by the disappearance of the 1.5-eV loss peak from the spectrum [Fig. III-5(d)], which is similar to the one for freshly broken TiO_2 [Fig. III-5(a)]. Subsequent O-ion sputter-etching of the TiO_2 surface of Fig. III-5(c) restores the spectrum of Fig. III-5(a), and Ar-ion sputter-etching of the Ti_2O_3 surface of Fig. III-5(d) restores the spectrum of Fig. III-5(b).

The 1.5-eV peak is also affected by simply exposing the surface to O_2, as shown by the loss spectra for TiO_2 and Ti_2O_3 on the left and right sides, respectively, of Fig. III-6(a-h). Figures III-6(a) and (b), respectively, are the spectra for an Ar-ion sputter-etched surface of TiO_2 and for a Ti_2O_3 surface broken in air. The other spectra were obtained after these surfaces had been exposed to O_2 pressures of 10^{-3} Torr [(c) and (d)], 10^{-2} Torr [(e) and (f)], and 10^{-1} Torr [(g) and (h)] for 10 minutes each. The 1.5-eV peak in the TiO_2 spectrum is reduced to a shoulder after exposure to only 10^{-3} Torr O_2, and disappears completely after exposure to 10^{-1} Torr O_2. The effect is smaller for the Ti_2O_3 sample, with the peak still about 30 percent of its initial height after exposure to 10^{-1} Torr O_2. The fact that O_2 has any effect at all on the Ti_2O_3 surface is surprising, since the samples had remained in air for several minutes after being broken because of the time required to mount them in the ultrahigh-vacuum system. Possibly, gases other than O_2 are adsorbed on the surface in air, inactivating some of the sites that could otherwise trap O, and these gases are removed during pumpdown in the vacuum system. For Ti_2O_3 surfaces that were sputter-etched with Ar ions before being exposed to O_2, the 1.5-eV peak decreased more rapidly with O_2 exposure than for the broken surface shown in Fig. III-6. This increased activity may be due to the disorder and broken bonds produced on the surface during sputter-etching.

We also have exposed TiO_2 and Ti_2O_3 surfaces to water vapor in the same manner as for O_2. Surfaces that exhibited no 1.5-eV peak initially were unaffected by exposure to water vapor. For Ar-ion sputter-etched surfaces of TiO_2, the dependence of the 1.5-eV peak height on water-vapor exposure was similar to that shown in Fig. III-6 for the O_2 exposure of Ti_2O_3. Ar-ion sputter-etched Ti_2O_3 showed a decrease of only 25 percent in 1.5-eV peak height after exposure to 10^{-1} Torr of water vapor.

We attribute the peaks in n(E) observed at 5.5, 10.0, and 13.5 eV for both TiO_2 and Ti_2O_3 (Figs. III-5 and III-6) to cross transitions from the ground state of the O^{2-} ion to the lowest Ti d-level, leaving the resulting O^- ion in one of three different excited ionic states. The main reason for this interpretation is that ESCA data[6] on H_2O and ultraviolet photoemission data[7] on SiO_2 and GeO_2 all show similar triplet structures. An alternative model[6] that explains the structure

in H_2O in terms of the M energy levels of the initial state is unlikely in view of the significant differences to be expected for such levels in H_2O, GeO_2, and SiO_2.

We propose that the peak in n(E) at 1.5 eV is due to the excitation of electrons between crystal-field-split levels of the $3d^1$ states of Ti^{3+} ions. This model correctly predicts the presence of the peak for freshly broken Ti_2O_3 surfaces, where the metal ions are Ti^{3+} ($3d^1$), and its absence for broken surfaces of TiO_2, where the ions are Ti^{4+} ($3d^0$). The appearance of the 1.5-eV peak after Ar-ion sputter-etching of TiO_2 surfaces is consistent with the decrease in the amount of O on the surface and the resulting reduction of some of the Ti^{4+} surface ions to Ti^{3+}. Also, the weakening or disappearance of the peak on exposure to O_2 or water vapor is consistent with the oxidation of Ti^{3+} surface ions to Ti^{4+}. The magnitude of the crystal-field splitting of the 3d levels necessary for this model, 1.5 eV, is fairly close to the value of 2.4 eV observed optically for Ti^{3+} in Al_2O_3 (see Ref. 8), and is consistent with an increase in the crystal-field splitting due to the smaller lattice constant of Al_2O_3.

If the 1.5-eV peak does, indeed, arise from the 3d levels of the Ti^{3+} ion, the excitation of the 3d electron to a 4s state on the Ti^{3+} ion would be expected to result in another peak at about 10 eV. This is in the middle of the valence-band triplet structure, and we have not been able to observe any additional peaks in that region that correlate with the presence of the 1.5-eV peak.

V. E. Henrich
G. Dresselhaus
H. J. Zeiger

C. PREPARATION OF Sn-DOPED In_2O_3 FILMS BY RF SPUTTERING

Because properly prepared films of Sn-doped In_2O_3 simultaneously have high values of electrical conductivity, visible transmission, and infrared reflectivity, these films are potentially useful in the collection and conversion of solar energy — in particular, as transparent heat mirrors for solar thermal collectors and as transparent electrodes for photovoltaic solar cells. In an attempt to obtain films of sufficient quality for practical use in these applications, we have developed a method for producing films by RF sputtering and have investigated the dependence of film properties on preparation conditions.

The techniques that have been used to prepare Sn-doped In_2O_3 films include chemical spray deposition, DC sputtering, and RF sputtering. In order to obtain satisfactory electrical and optical properties by any of these techniques, it is necessary either to heat the substrate during deposition or to anneal the film after deposition. Either procedure requires fairly high temperatures, typically over 500 °C. Our RF-sputtering method employs substrate heating rather than post-deposition annealing. The unusual feature of the method is that, by operating at sufficiently high power levels, heating is accomplished entirely by the electron bombardment intrinsic to RF sputtering, rather than by using an auxiliary resistance heater in the conventional manner.

Films of Sn-doped In_2O_3 were deposited on a variety of substrates — Corning Code 7059 glass, fused silica, sapphire, and CaF_2 — by sputtering in argon (10^{-2} Torr pressure) from a 12.5-cm-diameter, hot-pressed target of nominal composition In_2O_3 — 9 m/o SnO_2. The substrate was insulated from the water-cooled, stainless-steel substrate platform by means of a Pyrex spacer about 0.15 cm thick. The substrate temperature T_s was measured with a chromel-alumel thermocouple that was mounted on the substrate surface with kaolin-sodium silicate paste and protected from RF interference by suitable chokes. The value of T_s increased reproducibly with increasing RF power, reaching over 600 °C for 650 W, the maximum power used.

Both the electrical and optical properties of the films improved systematically with increasing T_s over the entire temperature range. As shown by Fig. III-7, the electrical resistivity decreased from about 10^{-3} ohm-cm for $T_s \approx 300\,^\circ$C to about 2×10^{-4} ohm-cm for $T_s \approx 650\,^\circ$C, and there is no indication of saturation at the highest temperature. (Figure III-7 also indicates the relationship between T_s and the RF power, since abscissa scales are given for both quantities.) Hall coefficient measurements showed that the decrease in resistivity was due to increases in both the carrier concentration and mobility, which reached values of about 8×10^{20} cm^{-3} and 40 cm^2/V-sec, respectively, at the maximum temperature. The conductivity is n-type.
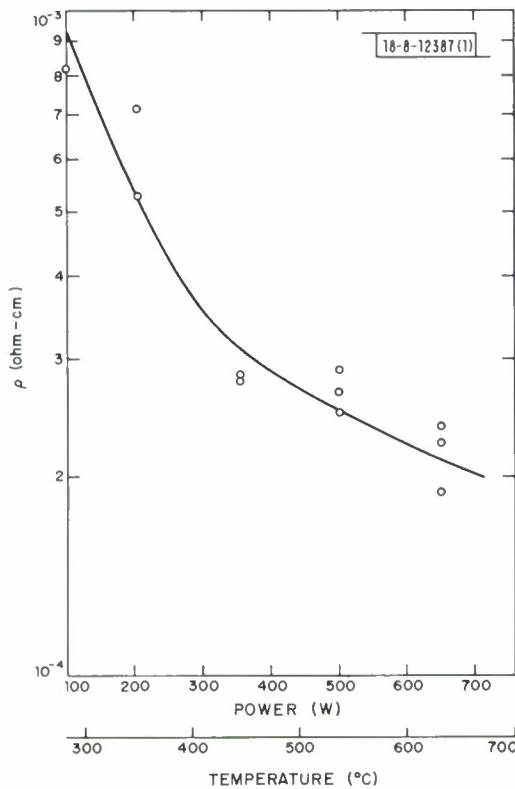
Fig. III-7. Variation of electrical resistivity (ρ) with substrate temperature and RF power for Sn-doped In_2O_3 films prepared by RF sputtering.
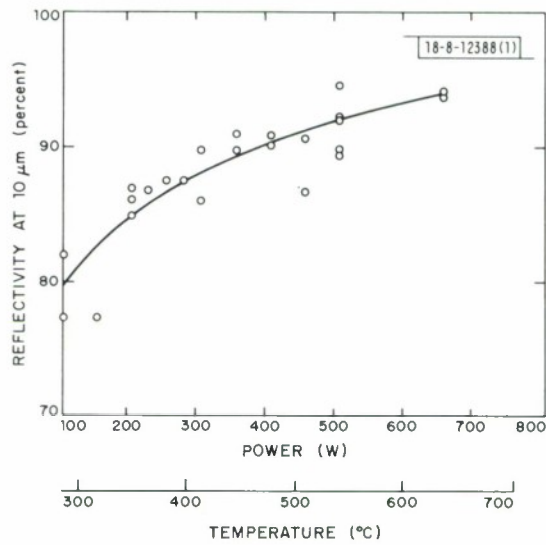
Fig. III-8. Variation of reflectivity at wavelength of 10 μm with substrate temperature and RF power for Sn-doped In_2O_3 films prepared by RF sputtering.

For optimum performance, transparent heat-mirror films should have the highest possible transmission in the visible region of the spectrum, the highest possible reflectivity in the infrared, and a sharp transition between the two regions at a wavelength of about 1 μm (see Ref. 9). Figure III-8 shows that the reflectivity at 10 μm increased with increasing T_s, reaching about 95 percent for $T_s \approx 650\,^\circ$C. For films deposited at this temperature, the visible transmission (corrected for substrate attenuation) exceeded 90 percent. Figure III-9 shows the results of detailed spectral measurements made over the wavelength range from 0.3 to 3 μm on a film deposited on glass at $T_s = 550\,^\circ$C.
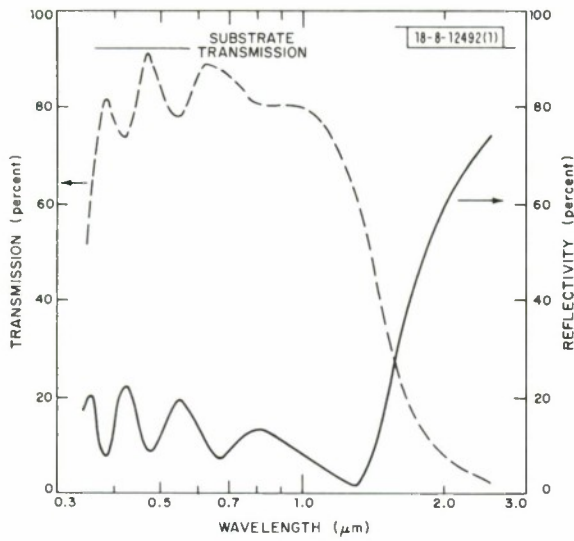
Fig. III-9. Variation of transmission and reflectivity with wavelength for Sn-doped In_2O_3 films deposited by RF sputtering on glass substrate heated to 550°C. Structure below 1 μm is due to interference effects.

TABLE III-1

COMPOSITION OF Sn-DOPED In_2O_3 FILMS PREPARED BY RF SPUTTERING

Sputtering Power (W)	Estimated Substrate Temperature T_s (°C)	Weight Percent			Atomic Percent		
		Sn†	In†	O‡	Sn	In	O
100	280	4.2	81.6	14.2	2.2	43.6	54.2
200	350	3.3	80.1	16.6	1.6	39.5	58.9
450	500	2.0	81.6	16.4	1.0	40.5	58.5
500	550	2.2	79.9	17.9	1.0	37.9	61.1

† Instrumental uncertainty is about 2 percent of the absolute value.

‡ Obtained by difference.

X-ray diffraction measurements show that the crystallites in the films exhibit some degree of preferred orientation. Films deposited on glass have a $\langle 100 \rangle$ fiber axis for low values of T_s, while they have a $\langle 111 \rangle$ fiber axis for high T_s. Films deposited at high T_s on fused silica, (0001) sapphire, and (111) CaF_2 have a variety of orientations. For a given T_s, however, the electrical and optical properties of the films are essentially independent of crystallite orientation and substrate.

Electron microprobe analysis has been used to determine the In and Sn contents of several films deposited at different RF power levels. The results are given in Table III-1. With increasing power (i.e., with increasing T_s), the Sn content generally decreases, although the carrier concentration increases.

J.C.C. Fan   P.M. Zavracky
F.J. Bachner   M.C. Finn
G.H. Foley

D. A NORMAL-INCIDENCE, ABSOLUTE REFLECTOMETER

The performance of transparent heat-mirror films (for example, the Sn-doped In_2O_3 films described in Sec. III-C) depends critically on the variation of their reflectance with wavelength.[9] Accurate reflectance data are therefore required for the design and evaluation of these films. In almost all reflectometers, however, measurements are made at "near-normal" incidence, and frequently the optical constants are such that the measured reflectances differ significantly from those for true normal incidence. (This is often the case for heat-mirror films in the wavelength region where the reflectance changes abruptly.) To remove this source of inaccuracy, we have designed and built a normal-incidence reflectometer. Instead of employing the usual relative method, which gives the ratio of the sample reflectance to the reflectance of a reference mirror, this instrument uses an absolute measurement technique that eliminates the possibility of errors due to changes in the reflectance of the reference mirror over extended periods of operation.

The essential features of the optical design are shown schematically in Fig. III-10. The sample reflectance at each wavelength is found by comparing the intensities of light beams from a monochromator that reach a photodetector by the two different optical paths shown. These are essentially equivalent except that the path on the left includes a reflection from the sample while the path on the right does not. Switching from one path to the other is accomplished by using a stepping motor to produce a $90° \pm 0.05°$ rotation of the beam-splitter assembly shown, which consists of three pieces of fused silica, all cut from the same 1-mm-thick plate, which are
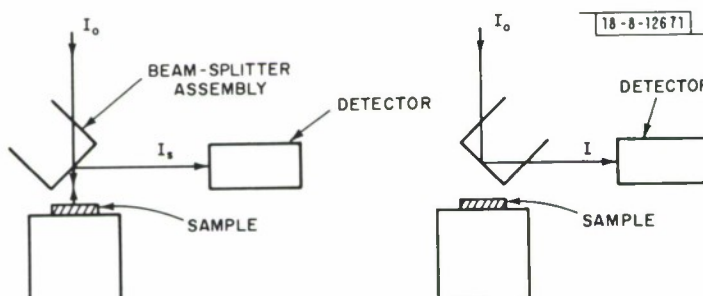
Fig. III-10. Basic optical design of normal-incidence reflectometer. Optical path at left includes reflection from sample, while path at right does not.

mounted so that they are perpendicular to each other to better than $1/3°$. It is easy to align the system so that both beams are incident on the same area of the detector.

For the optical path shown on the left side of Fig. III-10, the intensity (I_s) of the beam reaching the detector is given by

$$I_s = t^2 rRI_o \tag{III-3}$$

where t and r are, respectively, the transmittance and reflectance of each fused-silica plate, R is the sample reflectance, and I_o is the intensity of the incident beam from the monochromator. For the optical path shown on the right side, the intensity (I) of the beam reaching the detector is given by

$$I = t^2 rI_o \quad . \tag{III-4}$$

Comparison of Eqs. (III-3) and (III-4) shows that the sample reflectance is equal to the ratio I_s/I. (These equations ignore the attenuation of the two beams due to absorption by air, which is negligible in the visible and near-infrared for the pathlengths used. The difference in length between the two alternate paths is equal to twice the distance between the sample and the beam splitter, which is about 2 cm.)

The reflectance measurements are made at a series of fixed wavelengths, rather than by continuous scanning. At each wavelength, four intensity measurements (alternating between I_s and I) are obtained by making four rotations of the beam-splitter assembly, so that two independent reflectance values are determined. The drive motors for the monochromator and the beam-splitter assembly are controlled and synchronized by means of a logic control unit, which is shown together with the other principal components of the electronic system in the block diagram of Fig. III-11. As indicated in this diagram, the logic unit also controls the operation of the
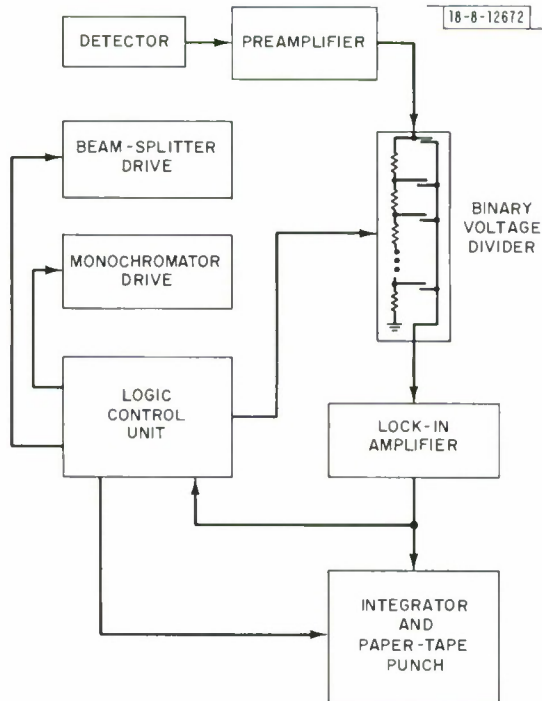
Fig. III-11. Block diagram of electronic system for normal-incidence reflectometer.

signal detection and recording components. The signals from the photodetector, which are modulated at 700 Hz by mechanically chopping the incident beam from the monochromator, are conditioned by means of a preamplifier and binary voltage dividers for processing by a lock-in amplifier. The preamplifier output is divided automatically by the voltage dividers, one for I_S and one for I, so that throughout an entire run the input voltage to the lock-in amplifier remains within a preset range – generally between 40 and 100 percent of one particular amplifier scale, so that errors due to switching from one scale to another are eliminated. The range of the dividers is adequate to compensate not only for changes in the sample reflectance with wavelength, but also for changes in the light source intensity and detector sensitivity that in conventional spectrophotometers are compensated by varying either the light source input power, the detector voltage, or the monochromator slit width. For each intensity measurement, the output from the lock-in amplifier is integrated for 1 sec by an integrator that records the result on paper tape. After a run is completed, a computer is used to reduce the data on the tape and to plot the measured reflectance values as a function of wavelength.

The reflectometer has a wide dynamic range, permitting reflectance values as low as 10^{-4} to be measured. The accuracy of the measurements depends largely on the quality of the beamsplitter assembly. The three members must have the same, uniform thickness, and they must be accurately perpendicular to each other. With our system, an accuracy of better than 1 percent of the absolute reflectance easily is achieved. The performance of the system is illustrated by the data plotted in Fig. III-12 for the reflectance of an aluminum mirror over the wavelength range from 0.2 to 2 μm. The measurements were made with a tungsten filament source and

Fig. III-12. Reflectivity of aluminum mirror vs wavelength. Values measured with normal-incidence reflectometer (points) are compared with National Bureau of Standards calibration curve.
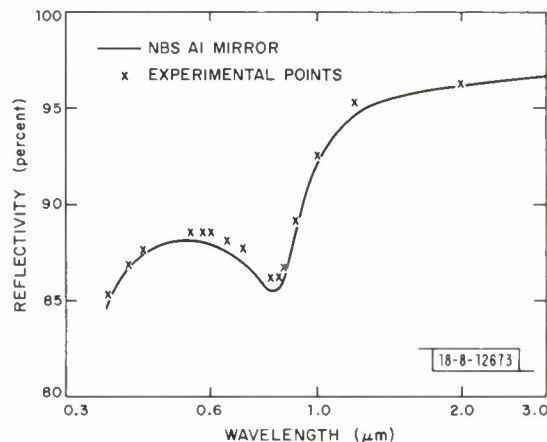
fused-silica prism monochromator. The detectors used were an S-20 photomultiplier, an S-1 photomultiplier, and a PbS cell. The agreement between the measured reflectance values (shown as points in Fig. III-12) and the calibration curve furnished by the National Bureau of Standards is never worse than 1 percent, and in many cases is much better. (The NBS measurements were made at an angle of incidence between 6° and 12°, but in this wavelength range the reflectance of aluminum is not very sensitive to the angle of incidence.)

<div align="right">
J.C.C. Fan
P.M. Zavracky
</div>
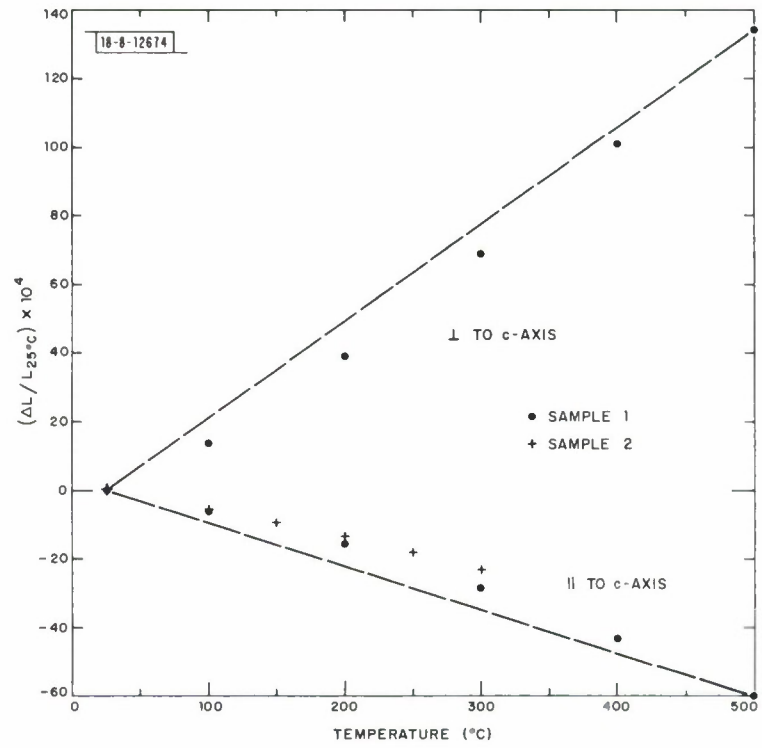
Fig. III-13. Thermal expansion of AgGaSe$_2$ parallel and perpendicular to c-axis.

E. POSITIVE AND NEGATIVE THERMAL EXPANSION COEFFICIENTS OF AgGaSe$_2$

Because of its large nonlinear optical coefficient, strong birefringence, and wide range of transparency (about 1 to 18 μm), the I-III-VI$_2$ compound AgGaSe$_2$ is one of the most effective materials currently available for frequency doubling and mixing in the infrared region of the spectrum.[10] In addition, its melting point (850°C) is low enough to permit convenient growth from the melt by the vertical Bridgman method in fused-silica ampoules. Utilization of the compound has been limited, however, because this growth method has had a low yield of single crystals of sufficient size and optical quality for nonlinear applications.

The principal problem in obtaining satisfactory crystals of AgGaSe$_2$ (and most other I-III-VI$_2$ and II-IV-V$_2$ compounds) has been the cracking of the melt-grown ingots. It has been assumed that cracking originates at grain boundaries, because of differences between the thermal expansion coefficients in different crystallographic directions. Such differences are to be expected because AgGaSe$_2$ has the tetragonal chalcopyrite structure, which is derived from the cubic zinc-blende structure by the random distribution of Ag and Ga atoms among the cation sites to produce a doubling of the c-axis.

On the basis of this explanation, we anticipated that cracking would not occur in single-crystal ingots. However, in recent attempts to grow crystals for frequency-mixing experiments, we found that in almost every run both the ingot and the growth ampoule were cracked and broken, even when the ingot appeared to be a single crystal. Further investigation showed that cracking failed to occur only in single crystals that had grown with their c-axis oriented within 20° of the axis of the Bridgman ampoule. (In contrast, no cracking occurred in single crystals of CdGeAs$_2$, another compound with chalcopyrite structure, regardless of their growth orientation.) This observation prompted a study of the thermal expansion of AgGaSe$_2$.

Dilatometer measurements of linear thermal expansion were made by the Dynatech R/D Company (Cambridge, Massachusetts) on two oriented samples cut from crack-free single crystals of AgGaSe$_2$ that we had grown by the Bridgman method. Measurements up to 500°C were made both parallel and perpendicular to the c-axis on Sample 1 (a cylinder 14 mm long and 16 mm in diameter), while the expansion parallel to the c-axis was measured up to 300°C on Sample 2 (6 × 6 × 19 mm). The results are shown in Fig. III-13, where the relative change in length for each orientation (i.e., the length at temperature T minus the length at 25°C, divided by the length at 25°C) is plotted against temperature. Not only is the thermal expansion seen to be strongly anisotropic, as expected, but the expansion coefficient parallel to the c-axis is actually negative. The occurrence of a negative coefficient in one crystallographic direction is quite unusual, but by no means unique. Trigonal Se and Te both have negative expansion coefficients parallel to the c-axis, and a negative coefficient much larger than the one for AgGaSe$_2$ recently has been observed[11] in the direction parallel to the c-axis in InBi, another compound with tetragonal structure.

The expansion-coefficient data provide a straightforward explanation of our observations on the cracking of Bridgman-grown single crystals of AgGaSe$_2$. As they cool to room temperature following solidification, these crystals contract in the usual manner in the direction perpendicular to the c-axis, but they expand in the direction parallel to the c-axis and along all directions within about 25° of the c-axis. Therefore, no force normal to the walls of the growth ampoule will result from the cooling of any crystal whose c-axis is parallel to the ampoule axis or makes an angle of less than 25° with the ampoule axis. For all other crystal orientations, however, the

TABLE III-2

FINAL ATOMIC PARAMETERS FOR $NdLiP_4O_{12}$ [†]

Space group C2/c; cell parameters: $a = 16.408(3)$ Å, $b = 7.035(4)$ Å, $c = 9.729(4)$ Å, $\beta = 126.38(5)°$

	x	y	z	β_{11}	β_{22}	β_{33}	β_{12}	β_{13}	β_{23}
Nd	0	0.1995(2)	1/4	0.0007(1)	0.0012(4)	0.0002(3)	0	0.0005(1)	0
Li	0	0	0	0.08(2)	0.18(9)	0.03(3)	0	0	0
P(1)	0.3617(4)	0.0562(8)	0.3368(7)	0.0011(3)	0.004(1)	0.002(1)	0.0005(5)	0.0011(5)	0.0002(9)
P(2)	0.1487(4)	0.1568(8)	0.0968(7)	0.0013(3)	0.001(1)	0.003(1)	0.0006(5)	0.0011(5)	0.0004(9)
O(1)	0.4342(9)	0.004(2)	0.297(1)	0.0008(8)	0.005(3)	0.002(2)	0.000(1)	0.000(1)	0.000(2)
O(2)	0.256(1)	0.088(2)	0.154(2)	0.0006(8)	0.007(3)	0.000(2)	0.000(1)	0.000(1)	0.000(2)
O(3)	0.385(1)	0.217(2)	0.451(2)	0.0021(9)	0.005(3)	0.000(2)	-0.002(1)	-0.001(1)	-0.002(2)
O(4)	0.161(1)	0.379(2)	0.086(2)	0.0023(9)	-0.002(3)	0.008(3)	0.000(1)	0.004(1)	0.000(2)
O(5)	0.4248(9)	0.401(2)	0.083(2)	0.0011(8)	0.006(3)	0.001(2)	0.000(1)	0.000(1)	0.000(2)
O(6)	0.132(1)	0.120(2)	0.225(2)	0.0029(9)	0.006(3)	0.006(3)	0.000(1)	0.005(1)	-0.002(2)

† Standard deviations are given in parentheses.

expansion along the c-axis (amounting to about 0.6 percent between 500°C and room temperature, the range of the dilatometer data) will produce a strong compressive force normal to the ampoule walls, consistently causing breakage of the ampoule and cracking of the crystal. A marked increase in the yield of crack-free crystals could therefore be achieved by finding experimental conditions which would ensure that the growth axis is parallel, or nearly parallel, to the c-axis.

<div align="right">G. W. Iseler</div>

F. CRYSTAL STRUCTURE OF $NdLiP_4O_{12}$

The concentration quenching of Nd^{+3} fluorescence is reduced markedly for compounds (e.g., NdP_5O_{14}) in which the Nd-O polyhedra are isolated from each other.[12] Because efficient radiative recombination occurs in these materials at very high Nd concentrations, they can be used for low-threshold, miniature lasers that are potentially useful in integrated optics and optical communications. The latest Nd compound reported to exhibit reduced concentration quenching is $NdLiP_4O_{12}$, for which Yamada, Otsuka, and Nakano[13] have obtained pulsed laser action and we have obtained CW laser action.[14] In order to check whether this compound too has isolated Nd-O polyhedra, we have determined its crystal structure by x-ray diffraction.

Instead of growing the crystals by the Kyropoulos pulling technique,[13] we have used a flux method. The starting materials were reagent grade Li_2CO_3, $NH_4H_2PO_4$, and Nd_2O_3, with a large excess of the first two compounds used as a flux. In a typical run, 11 g of Li_2CO_3, 86 g of $NH_4H_2PO_4$, and 20 g of Nd_2O_3 were mixed in a 50-cm^3 Pt crucible, preheated at 200°C for 4 hours, and fired at 950°C overnight. The temperature was then reduced at 2°/h to 700°C and the power was turned off. The crystals are typically diamond-shaped platelets about 0.2 mm thick and 0.5 mm on a side, with the broad face a (001) plane and the diagonals of the face lying along the a- and b-directions.

For x-ray diffraction studies, a small crystal 0.05 mm thick and about 0.3 mm on a side was aligned along the b-axis. Oscillation and Weissenberg photographs showed diffraction symmetry 2/m, instead of the mmm symmetry reported.[13] The cell parameters obtained from single-crystal diffractometer measurements are a = 16.408(3) Å, b = 7.035(4) Å, c = 9.729(4) Å, β = 126.38(5)° with space group C2/c.

Three-dimensional intensity data to 2Θ = 50° were collected in the manner described previously.[15] A total of 590 independent reflections were measured. The heavy-atom method was used to solve the structure. Since there are four Nd atoms in the unit cell, they should occupy a special position of space group C2/c. A three-dimensional Patterson map showed a strong peak at (0, 0.40, 1/2), which immediately suggests that the Nd site is 4e (0, 0.20, 1/4). A least-squares program based on this position gave R = 0.36. A difference Fourier map based on this model clearly revealed two independent P and six independent O positions. The Li position is difficult to locate by x-ray data. The 4a (0, 0, 0) position was selected because it is the only one of the four possible special positions that gives reasonable Li-O distances. The atomic positions and anisotropic temperature factors were then refined. Their final values are listed in Table III-2, and the bond distances and angles are listed in Table III-3. For all reflections, R = 0.072 and Rw = 0.077.

The structure of $NdLiP_4O_{12}$ is illustrated in Figs. III-14 and III-15. The basic structural units are helical ribbons, $(PO_3)_n$, formed by corner-sharing of PO_4 tetrahedra. (Therefore, the compound should be designated as a metaphosphate rather than as an ultraphosphate, the

TABLE III-3
BOND DISTANCES AND ANGLES FOR NdLiP$_4$O$_{12}$[†]

Dodecahedron Around Nd			
	Distances (Å)		Angles (deg)
Nd – O(1)	2 × 2.56(1)		
Nd – O(3)	2 × 2.42(1)		
Nd – O(5)	2 × 2.49(1)		
Nd – O(6)	2 × 2.38(1)		

Rectangle Around Li			
Li – O(5)	2 × 1.96(1)	O(5) – Li – O(6)	102.8(6)
Li – O(6)	2 × 2.141(1)	O(5) – Li – O(5)	180.0
		O(6) – Li – O(6)	180.0

Tetrahedron Around P(1)			
P(1) – O(1)	1.50(1)	O(1) – P(1) – O(2)	104.5(7)
P(1) – O(2)	1.60(1)	O(1) – P(1) – O(3)	119.6(8)
P(1) – O(3)	1.47(1)	O(1) – P(1) – O(4)	111.7(8)
P(1) – O(4)	1.61(1)	O(2) – P(1) – O(3)	110.9(8)
		O(2) – P(1) – O(4)	103.2(8)
		O(3) – P(1) – O(4)	105.8(8)

Tetrahedron Around P(2)			
P(2) – O(2)	1.57(1)	O(2) – P(2) – O(4)	99.6(7)
P(2) – O(4)	1.59(1)	O(2) – P(2) – O(5)	106.9(8)
P(2) – O(5)	1.48(1)	O(2) – P(2) – O(6)	112.5(8)
P(2) – O(6)	1.45(1)	O(4) – P(2) – O(5)	103.9(8)
		O(4) – P(2) – O(6)	109.2(8)
		O(5) – P(2) – O(6)	122.1(8)

Inter-cation Distances and Inter-tetrahedron Angles			
P(1) – P(2)	2.93(8)	P(2) – O(2) – P(1)	133(1)
Nd – Nd	2 × 6.642	P(2) – O(4) – P(1)	131(1)
Nd – Nd	2 × 6.440		
Nd – Nd	2 × 5.620		
Nd – Li	2 × 2.808(1)		

† Standard deviations are given in parentheses.
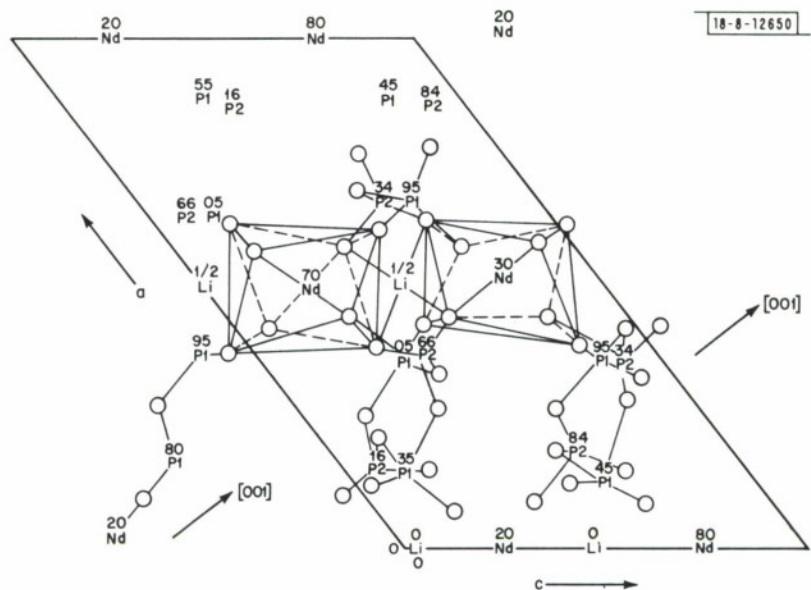
Fig. III-14. Crystal structure of $NdLiP_4O_{12}$ projected in a-c plane.
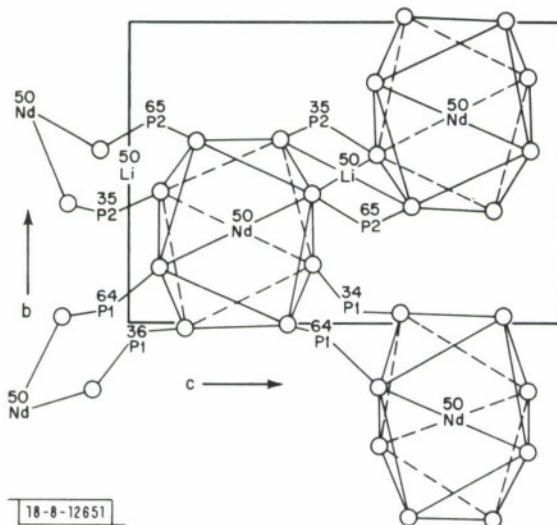
Fig. III-15. Crystal structure of $NdLiP_4O_{12}$ projected in b-c plane.

18-8-12651

nomenclature adopted in Ref. 13.) The ribbons run along the b-axis and are joined to each other by NdO_8 dodecahedra. Each NdO_8 dodecahedron is surrounded by four others. As shown in Fig. III-15, it is connected to two of these by two P(1) atoms, with a Nd-Nd distance of 6.440 Å, while it is connected to the other two by a Li atom as well as by two P(2) atoms, with a shorter Nd-Nd distance of 5.620 Å. However, the NdO_8 dodecahedra are isolated from each other in the sense that they do not share any O atoms. This type of isolation is the structural feature that is common to all the Nd compounds exhibiting reduced concentration quenching.

H. Y-P. Hong

53

REFERENCES

1. A. Fujishima and K. Honda, Nature $\underline{238}$, 37 (1972).

2. Solid State Research Report, Lincoln Laboratory, M.I.T. (1974:2), p. 32, DDC AD-783634/9.

3. J. F. Dewald, in The Surface Chemistry of Metals and Semiconductors, H.C. Gatos, Ed. (J. Welegand Sons, Inc., New York, 1960), p.205.

4. D.I. Tchernev (to be published).

5. A. Frova, P.J. Boddy and Y.S. Chen, Phys. Rev. $\underline{157}$, 700 (1967).

6. K. Siegbahn, et al., ESCA Applied to Free Molecules (North-Holland Publishing Company, Amsterdam, 1969), p.83.

7. J.E. Rowe, Appl. Phys. Lett. $\underline{25}$, 576 (1974).

8. D.S. McClure, Phys. Rev. $\underline{36}$, 2757 (1962).

9. J.C.C. Fan, T.B. Reed and J.B. Goodenough, in Proceedings of the 9th Intersociety Energy Conversion Engineering Conference, San Francisco, 1974 (Society of Automotive Engineers, Inc., New York, 1974), p.341.

10. H. Kildal and J.C. Mikkelsen, Opt. Commun. $\underline{9}$, 315 (1973), DDC AD-777560/4.

11. T.J. White, J.H. Davis and H.U. Walter, J. Appl. Phys. $\underline{46}$, 11 (1975).

12. H.Y-P. Hong and K. Dwight, Mater. Res. Bull. $\underline{9}$, 775 (1974), DDC AD-786294/9.

13. T. Yamada, K. Otsuka and J. Nakano, J. Appl. Phys. $\underline{45}$, 5096 (1974).

14. S.R. Chinn and H.Y-P. Hong (to be published).

15. H.Y-P. Hong, Acta Crystallogr. $\underline{B30}$, 468 (1974), DDC AD-A000491/1.

IV. MICROELECTRONICS

A. VERS-11 SENSOR

Work on the VERS-11 (Visible Earth Radiation Sensor)[1] for use in the stationkeeping systems of the LES-8/9 satellites is nearly complete. Three flight units have been delivered to the Spacecraft Technology Group, a fourth unit is ready for delivery, and two more units are in the final stages of assembly. The sensor is a hybrid integrated circuit consisting of four silicon photodiode arrays mounted on a 2- × 2-inch alumina substrate (Fig. IV-1). Each diode array contains
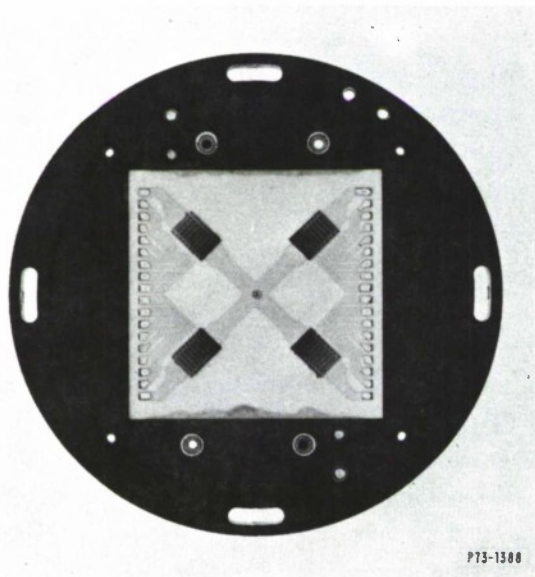
Fig. IV-1. Front view of completed VERS-11. Four 8-element silicon photodiode arrays are shown mounted on metalized aluminum substrate which is epoxied to anodized aluminum plate.
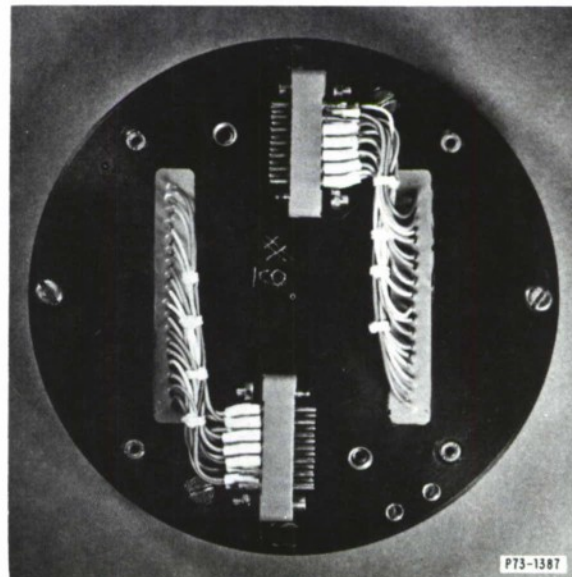
Fig. IV-2. Back view of completed VERS-11 shown in Fig. IV-1. In this view, connectors which mate with external circuitry may be seen.

eight photodiodes optimized for operation in the visible portion of the spectrum. The alumina substrate is mounted on an aluminum backing plate, and wires are soldered to the metalization on the substrate and terminated at connectors which are bolted to the backing plate (Fig. IV-2). Details of the fabrication of the hybrid integrated circuit and its incorporation into the completed sensor are as follows:

(1) The individual diodes in each array are shallow junction (1.3 μm) n^+-p photosensitive junctions on high-resistivity (5-ohm-cm) p-type silicon wafers. The diodes are separated by a p^+-channel stop, and the edges of the diodes are shielded with metalization to eliminate spurious edge responses. The metalization on the diode arrays is electron-beam evaporated Ti/Pd/Au.

(2) The ceramic substrate is as-fired, 99.5-percent alumina with an 8- to 10-microinch surface finish. The dimensions of the substrate are 2 × 2 × 0.025 inches. The holes into which the wires to the connectors are soldered are laser drilled.

(3) The substrates are metalized front and back by sputtering Ti/Pd/Au and the gold electroplated to a thickness of 2.5 µm. The metalization is patterned by simultaneously laminating the front and back of the substrate with sheet photoresist, exposing the resist with the required masks, developing, baking, and etching. The metalization on the back of the substrate (not shown) is simply a square surrounding each hole to facilitate soldering.

(4) Diode arrays are mounted on the substrate using a gold-filled epoxy. The arrays are precisely aligned in X, Y, and Θ before the epoxy is cured. Connections are made from the metalization on the diodes to the substrate metalization with thermocompression bonded gold wires.

(5) Braided, insulated wire is soldered into the plate through holes in the substrate using a solder with a low solubility for gold. The substrate is then mounted on the aluminum backing plate using an insulating epoxy which is vacuum degassed before curing. The slots in the backing plate are filled with a space-qualified silicone potting compound used in conjunction with a primer to insure adhesion of the silicone to the aluminum. The final assembly step is to solder the wires into the connectors and bolt the connectors to the backing plate.

Details on tests on the survivability of the unprotected hybrid integrated circuit, which is the heart of the sensor, have been reported elsewhere.[2] In summary, the Ti/Pd/Au metalization in combination with gold wires and thermocompression bonding is extremely corrosion resistant, and the gold-filled epoxy used to bond the diode arrays to the substrate will survive for extended periods at 125°C — which is a substantially higher temperature than the maximum of 40°C that this epoxy will see in operation. Tests performed on the completed sensor include the LES-8/9 shake test and a thermal test wherein the sensor is tested at −60° and +80°C. The sensor has passed both these tests, and the optical and electrical performance of the hybrid integrated circuit has proven to be unaffected by the processing required to incorporate it into the complete sensor.

F. J. Bachner   L. L. Grant
R. A. Cohen   W. H. McGonagle
T. F. Clough   R. W. Mountain

B. CHARGE-COUPLED IMAGING ARRAYS

During the past quarter, two significant changes have been made in the fabrication of the charge-coupled devices for the TDAR Program (Telescopic Detection and Ranging).[3] Also, buried-channel devices have been made with improved transfer inefficiency.

The first process change involves the effects of N_2 and H_2 on the fixed oxide charge (Q_{ss}) and fast interface state density (N_{ss}). Although initial devices had a satisfactorily low Q_{ss} (5×10^{10} q cm^{-2}) using our N_2 annealing process, these same devices had an N_{ss} value (2×10^{11} cm^{-2} eV^{-1}) that was too large. Therefore, experiments were carried out using hydrogen annealing at various points in the process and at different temperatures.

These experiments clearly demonstrated that the final high-temperature fabrication process must be done in a H_2 ambient in order to achieve low interface state densities. The resulting N_{ss} values varied with final anneal temperature from 2×10^{10} cm^{-2} eV^{-1} at 1100°C to 4×10^{10} cm^{-2} eV^{-1} at 950°C without changing the Q_{ss} value which remained at 5×10^{10} q cm^{-2}.

The second process change involves the deposition of the polycrystalline silicon used for the overlapping gates. Because the original polysilicon deposition at 1000°C produced films with grain sizes that were too large for the present device, several tests were performed using low deposition temperatures (650° to 750°C) and a N_2 instead of a H_2 ambient. The film quality was found to be very dependent on the amount of moisture in the N_2. Even moisture levels as low as 3 ppm were found to affect several polysilicon characteristics, such as a tendency to produce films that were amorphous, had uneven growth, and higher resistivity after doping. By reducing the H_2O content to ~1 ppm, films of satisfactory quality have been produced.

Measurements of charge-transfer efficiency have continued during the past quarter. A 100-element serial surface-channel device was tested, and a transfer inefficiency of $\epsilon = 5 \times 10^{-3}$ per transfer was obtained at 0.5 MHz. This loss is due to fast interface state trapping, and a method described by Carnes and Kosonocky[4] was used to obtain a value for the interface state density of $N_{ss} = 1.3 \times 10^{10}$ cm^{-2} eV^{-1}. This represents an effective density of levels over some energy range in the upper half of the band gap.

With the addition of a background charge or fat zero, the inefficiency dropped to 1×10^{-3}. The remaining losses can be attributed to interface states at the edges of the potential wells.[5] Because the potential wells have sloping sides, any fat-zero charge accumulates in the center of a well and does not fill the interface states at the edges. The fat zero is therefore ineffective in reducing signal losses into these states. The problem is most severe when the channel is narrow and the substrate resistivity is high. Both conditions exist in these devices (channel width = 1.0 mil, $N_A = 3 \times 10^{14}$ cm^{-3}), and calculations[5] show that the remaining loss of $\epsilon = 1 \times 10^{-3}$ can be accounted for by the edge effect.

The major emphasis of this program has been placed on obtaining high-performance buried-channel devices, since it was known at the outset that the surface-channel device could not provide sufficiently high transfer efficiency. The program goal of a large-area, low-light-level imager requires $\epsilon \lesssim 8 \times 10^{-5}$. During the past quarter, we have tested a 100-element device with $\epsilon = 2 \times 10^{-4}$ at 1.0 MHz. This device was implanted with 5×10^{11} cm^{-2} phosphorus which was subsequently driven by thermal diffusion to a junction depth of about 1.5 μm.

R.A. Cohen   W.H. McGonagle
B.E. Burke   R.W. Mountain

C.   A SILICON SCHOTTKY-DIODE ARRAY FOR AN ACOUSTIC MEMORY AND CORRELATOR DEVICE

An acoustic correlator with memory has been successfully fabricated using the interaction between surface acoustic waves in lithium niobate and an array of Schottky barrier diodes on a silicon strip in close proximity (~0.1-μm gap) to the LiNbO$_3$ surface. In this section a brief description of the complete device will be given, and the details of the silicon diode array fabrication discussed.

The principle of this device is to image an acoustic surface-wave field by a differential charging of a pattern of Schottky diodes on a silicon strip adjacent to a lithium niobate surface-wave delay line. In operation, the Schottky barrier diodes are biased in the forward direction for a short period of time by a 600-V DC pulse applied across the structure of the silicon and the lithium niobate. During this time, the Schottky diodes acquire a charge which will be spatially modulated by the electric field of the acoustic surface wave on the lithium niobate. After the bias voltage is turned off, this charge will persist for a time determined by the leakage

through the Schottky barriers. The charge distribution on the Schottky diodes will give rise to a spatially varying depletion of the silicon which is an image of the acoustic field written in by the short DC pulse. This information can be read out by scanning an acoustic signal through the delay line and monitoring the acoustoelectric voltage induced across the silicon-lithium niobate structure. This output signal will be the correlation between the stored signal and the signal injected for the reading process. Preliminary experiments at 70 MHz have demonstrated the principle. Storage times of 10 msec have been observed with a writing pulse of 50 nsec. The loss in the writing process was −11 dB, whereas the loss in the reading process was comparable to regular acoustoelectric convolver loss, −60 dB.

The present diode array fabrication procedure starts with 30 ohm-cm, n-type, phosphorous-doped silicon wafers with a $\langle 100 \rangle$ orientation. An initial oxide of 1000 Å was thermally grown at 1100°C in dry O_2, and a chemically vapor-deposited (CVD) SiO_2 layer 5000 Å thick was deposited at 400°C in a N_2 ambient to protect the surface from subsequent diffusions. The back side was then lapped and etched to a final wafer thickness of 9 mils. A phosphorous deposition and diffusion at 1000°C was performed to produce a heavily doped layer ($C_s \sim 5 \times 10^{20}/cm^3$) of about ~ 3-μm final depth for an ohmic contact to the sample. Next, the front CVD and thermal SiO_2 were stripped in HF and a new MOS oxide 1000 Å thick was grown at 1100°C. Holes 0.2 mil on 0.5-mil centers were photolithographically produced and etched into the SiO_2. 2000 Å of Pt was sputtered onto the wafer and sintered into the silicon at 600°C for 15 minutes to form the PtSi Schottky barriers. The excess Pt was etched away with aqua regia. A 1000-Å/500-Å Cr/Au layer was then filament evaporated onto the entire wafer surface and pads were photolithographically patterned and etched to form 0.3-mil contact pads which cover the PtSi Schottky barrier diodes and overlap the neighboring MOS oxide. The back-side oxide was removed with HF and a 2000-Å Cr/3000-Å Au layer was filament evaporated onto the back side of the sample for ohmic contact. The finished convolver strips, 800×100 mils, were then scribed and broken along the $\langle 110 \rangle$ planes.

Although the results, 10-ms storage times and −11 dB loss, were extremely encouraging, there was a substantial nonuniformity in the correlation output that was related to a nonuniform doping in the silicon strip. New devices currently are being made using more uniform silicon wafers.

R. A. Cohen
R. W. Mountain
K. Ingebrigtsen

D. TAPPED DELAY LINE

Work has begun on the design and fabrication of a tapped delay line for the R.F. Systems Group under the Re-entry Systems Program. The maximum delay is 66 μsec, and there are a total of eleven taps (each with a different delay time) with nonuniform spacing. Since the unit ultimately will be used in a brassboard of a flight package, minumum size and weight of the packaged delay line are important considerations.

The desired specifications are summarized below:

3-dB bandwidth	100 MHz
Center frequency	300 MHz
Maximum delay	66 μsec
Number of taps	11
Insertion loss	50 dB maximum

Matching between taps	±2 dB maximum
Delay accuracy	±0.1 μsec
Spurious responses	−20 dB maximum
Material	$LiNbO_3$

Because several of the above requirements are similar to those of a delay line already fabricated by Hughes Aircraft Company,[6] we have used their design as a starting point for this device. The most difficult of these specifications is the 100-MHz bandwidth, and the bandwidth requirement is further complicated by the frequency dependence of the propagation loss in the $LiNbO_3$, which changes by almost 5 dB over 100 MHz for a 66-μsec delay. The above-mentioned Hughes device utilizes a special phase-reversal transducer which has unusually wide bandwidth and can be modified to give a tilted frequency response characteristic in order to compensate for the variation in propagation loss with frequency.

A total delay of 66 μsec requires a path length in lithium niobate of 9.056 inches, which is too long to fit in the space allotted for this device and which would be difficult to work with in any case. Two shorter (33-μsec) 4.5-inch-long delay lines in cascade are therefore used to obtain the desired maximum delay, which requires that each shorter delay line have a 1.5-dB bandwidth of 100 MHz.

The first step in the design of this delay line was the selection of the transducer types. It was decided to use a phase-reversal transducer (PRT) for the input, and uniform transducers for the output taps. Theoretical calculations indicated that an 11-finger PRT in conjunction with a 6-finger periodic transducer would provide the desired frequency response. However, a 6-finger transducer has an expected reflection coefficient of −19.3 dB, which would not meet the spurious response specification of −20 dB. For this reason, a 5-finger output transducer with a reflection coefficient near −21 dB was selected.

In order to check the theoretical calculations of transducer frequency response, two 7.5-μsec delay lines with two output taps were fabricated. One of these units was made with a gold-based metalization in order to investigate the suitability of this potentially more reliable material, and the other was made with aluminum. Besides appearing to be more difficult to fabricate with the metal lift techniques, the gold device had less bandwidth, a lower center frequency, and higher insertion loss. For these reasons, we have decided to use aluminum metalization for further work on surface-wave devices.

The device fabricated with aluminum metalization met all the desired specifications except for a 2- to 3-dB dip at the center of the passband. This dip is caused by the PRT and was expected to be about 1.3 dB. Work is continuing to find the cause of this discrepancy and to reduce the dip to 1.5 dB or less.

<div style="text-align:right">

D. L. Smythe
F. J. Bachner
R. C. Williamson

</div>

REFERENCES

1. Solid State Research Reports, Lincoln Laboratory, M.I.T. (1973:4), p. 69, DDC AD-778086/9; and (1974:1), p. 73, DDC AD-779823/4.

2. F. J. Bachner, R. A. Cohen, R. W. Mountain, W. H. McGonagle and A. G. Foyt, IEEE Trans. Parts, Hybrids, and Packaging PHP-10, 188 (1974).

3. Solid State Research Report, Lincoln Laboratory, M.I.T. (1974:4), p. 55, DDC AD-A004763.

4. J. E. Carnes and W. F. Kosonocky, Appl. Phys. Lett. 20, 261 (1972).

5. W. F. Kosonocky and J. E. Carnes, "Advanced Investigation of Two-Phase Charge-Coupled Devices," RCA Laboratories (May 1973), NASA CR-132304.

6. P. B. Snow, "Burst Processor Tapped Delay Line," Final Report, Hughes Aircraft Company (May 1974).

REPORT DOCUMENTATION PAGE		READ INSTRUCTIONS BEFORE COMPLETING FORM
1. REPORT NUMBER ESD-TR-75-118	2. GOVT ACCESSION NO.	3. RECIPIENT'S CATALOG NUMBER
4. TITLE *(and Subtitle)* Solid State Research		5. TYPE OF REPORT & PERIOD COVERED Quarterly Technical Summary, 1 November 1974 – 31 January 1975
		6. PERFORMING ORG. REPORT NUMBER
7. AUTHOR*(s)* McWhorter, Alan L.		8. CONTRACT OR GRANT NUMBER*(s)* F19628-73-C-0002
9. PERFORMING ORGANIZATION NAME AND ADDRESS Lincoln Laboratory, M.I.T. P.O. Box 73 Lexington, MA 02173		10. PROGRAM ELEMENT, PROJECT, TASK AREA & WORK UNIT NUMBERS Project No. 649L
11. CONTROLLING OFFICE NAME AND ADDRESS Air Force Systems Command Andrews AFB Washington, DC 20331		12. REPORT DATE 15 February 1975
		13. NUMBER OF PAGES 76
14. MONITORING AGENCY NAME & ADDRESS *(if different from Controlling Office)* Electronic Systems Division Hanscom AFB Bedford, MA 01731		15. SECURITY CLASS. *(of this report)* Unclassified
		15a. DECLASSIFICATION DOWNGRADING SCHEDULE

16. DISTRIBUTION STATEMENT *(of this Report)*

Approved for public release; distribution unlimited.

17. DISTRIBUTION STATEMENT *(of the abstract entered in Block 20, if different from Report)*

18. SUPPLEMENTARY NOTES

None

19. KEY WORDS *(Continue on reverse side if necessary and identify by block number)*

solid state devices	photodiode devices	imaging arrays
quantum electronics	lasers	surface wave transducers
materials research	laser spectroscopy	EAP detectors
microelectronics	infrared imaging	

20. ABSTRACT *(Continue on reverse side if necessary and identify by block number)*

This report covers in detail the solid state research work of the Solid State Division at Lincoln Laboratory for the period 1 November 1974 through 31 January 1975. The topics covered are Solid State Device Research, Quantum Electronics, Materials Research, and Microelectronics. The Microsound work is sponsored by ABMDA and is reported under that program.

DD FORM 1473
1 JAN 73   EDITION OF 1 NOV 65 IS OBSOLETE